Journal of Materials Research and Technology 45 (2026) 399–421

Contents lists available at ScienceDirect

Journal of Materials Research and Technology

journal homepage: www.elsevier.com/locate/jmrt

Integrated regulation of preparation-microstructure-properties for W/Mo refractory alloys and their composites

Yijia Wang [a], Rui Shu [a,*], Hongliang Sun [a], Yiran Mao [b], Jan W. Coenen [b], Chongyang Liu [b], Zheng Zhong [c], Xiaosong Jiang [a,**]

[a] *Key Laboratory of Advanced Technologies of Materials (Ministry of Education), School of Materials Science and Engineering, Southwest Jiaotong University, Chengdu, Sichuan, 610031, China*

[b] *Forschungszentrum Jülich GmbH, Institute of Fusion Energy and Nuclear Waste Management, Plasma Physics IFN-1, Jülich, 52428, Germany*

[c] *Institute for Applied Materials (IAM), Karlsruhe Institute of Technology (KIT), Kaiserstrasse 12, Karlsruhe, 76131, Germany*

ARTICLE INFO

Keywords:
Tungsten
Molybdenum
Strengthening and toughening mechanisms
Microstructure design

ABSTRACT

As representative Group 6 refractory metals, tungsten (W) and molybdenum (Mo) are promising candidates for aerospace, nuclear fusion, and other advanced engineering applications because of their extremely high melting points, excellent high-temperature strength, and high thermal conductivity. Their wider engineering use, however, is constrained by processing difficulties and limited service reliability, which are largely associated with intrinsic room-temperature brittleness and a high ductile-to-brittle transition temperature (DBTT). This review systematically examines recent advances in W- and Mo-based refractory alloys and composites within an integrated processing–microstructure–property framework. First, melting, powder metallurgy, and additive manufacturing are compared in terms of their respective advantages and limitations in impurity control, grain refinement, and densification. Second, homogeneous and heterogeneous microstructural architectures are reviewed and compared, together with different modes of interfacial bonding and the patterns of microstructural evolution under different thermodynamic and kinetic conditions. Particular emphasis is placed on interpreting strengthening and toughening mechanisms from the perspective of crystal defects of different dimensionalities and on analyzing irradiation-damage behavior, thereby supporting the reliable engineering deployment of W- and Mo-based materials in extreme environments. Finally, future research priorities are summarized, including standardized multi-property evaluation, characterization and testing under coupled multiphysics conditions, multiscale simulation, and component-scale validation.

1. Introduction

Continued advances in modern industry and technology have placed increasingly stringent demands on materials used in extreme service environments. Plasma-facing materials (PFMs) for fusion reactors [1–3], divertor structural materials [4,5], nuclear reactor cladding materials [6,7], and advanced aerospace components, such as rocket nozzles and hypersonic aircraft components [8,9], are exposed to extremely high temperatures, severe thermal shock, high-flux particle irradiation, and complex cyclic loading. These materials must therefore retain their structural integrity and mechanical performance under such conditions. Among the candidate materials, tungsten (W) and molybdenum (Mo) are particularly attractive because both are refractory metals with a body-centered cubic (BCC) crystal structure. Their suitability for extreme environments derives from their high melting points (3422 °C for W and 2620 °C for Mo), high strength and structural stability at elevated temperatures, good thermal conductivity, low coefficients of thermal expansion, and low sputtering yields [1,10,11] (Fig. 1).

Despite their outstanding properties at elevated temperatures, W and Mo possess inherent physical and metallurgical limitations that remain major barriers to their broader engineering application. In the BCC lattice, the nonplanar cores of $1/2\langle 111\rangle$ screw dislocations give rise to a high Peierls stress that impedes dislocation glide [12]. The resulting lattice resistance suppresses dislocation glide at low temperatures, contributing to pronounced room-temperature brittleness and a high ductile-to-brittle transition temperature (DBTT), which has been

* Corresponding author.
** Corresponding author.
E-mail addresses: r.shu@swjtu.edu.cn (R. Shu), xsjiang@swjtu.edu.cn (X. Jiang).

https://doi.org/10.1016/j.jmrt.2026.09.068
Received 7 August 2026; Received in revised form 7 September 2026; Accepted 7 September 2026
Available online 9 September 2026

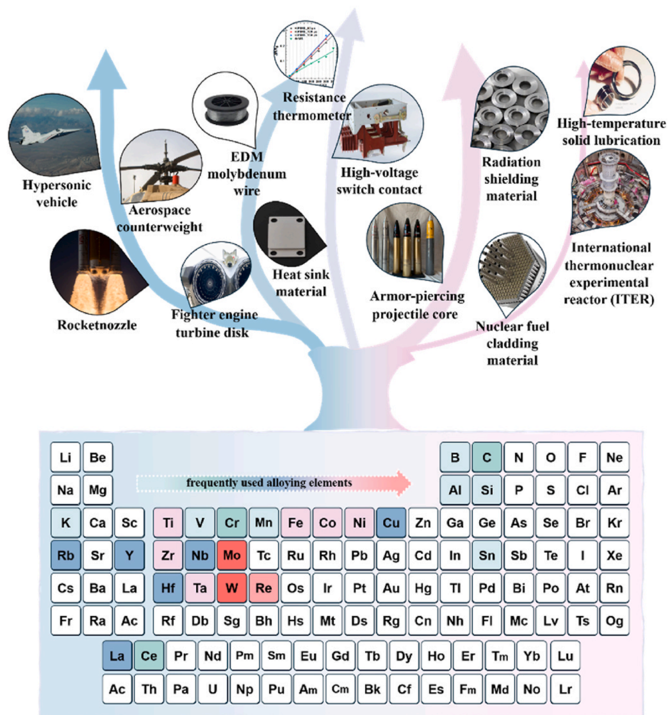

Fig. 1. Applications of W/Mo alloys and composites and their common additive elements.

reported to be approximately 400 °C for pure W. W and Mo are also highly sensitive to interstitial impurities, particularly oxygen (O), nitrogen (N), and carbon (C). These impurities readily segregate to grain boundaries and weaken grain boundary cohesion, thereby promoting intergranular brittle fracture under applied loading [8,13]. During processing or service, exposure to elevated temperatures can also induce recrystallization in W- and Mo-based materials. The accompanying grain coarsening reduces strength and may lead to recrystallization-induced embrittlement. Energetic particle irradiation generates defects such as dislocation loops and voids, which contribute to irradiation hardening and mechanical property degradation [3,5,7]. In W, irradiation may also cause damage phenomena such as surface fuzz formation and volumetric swelling [14]. Collectively, these limitations complicate the machining and forming of W- and Mo-based materials, hinder the fabrication of complex components, and restrict their broader engineering application.

To address these limitations, recent research has focused on processing innovation, compositional and microstructural design, and the mechanisms governing property optimization in W- and Mo-based materials. In processing, conventional powder metallurgy (PM) and melting routes remain widely used, although they often involve a trade-off between densification and grain coarsening. The emergence of additive manufacturing (AM), commonly known as three-dimensional (3D) printing, has enabled the near-net-shape fabrication of geometrically complex W- and Mo-based components [15–20]. However, the steep thermal gradients and rapid cooling rates inherent to AM can generate high residual stresses [21,22], resulting in microcracking and, in severe cases, macroscopic cracking. Crack suppression therefore remains a major challenge in the AM of refractory metals. For compositional and microstructural design, second-phase dispersion strengthening with oxides or carbides [23–26], alloying [27,28], and grain refinement, including nanocrystalline (NC) strengthening [9,14,29–31], have been widely adopted. These strategies seek to promote strength-toughness synergy while enhancing irradiation resistance and high-temperature stability under extreme conditions [32,33]. Despite substantial progress, several challenges remain, including the limited availability and high cost of certain alloying elements, second-phase coarsening at elevated temperatures, and particle agglomeration. Accordingly, current research is increasingly focused on precise microstructural control. One approach is to develop homogeneous microstructures containing uniformly dispersed nanoscale phases and tailored coherent or semi-coherent interfaces [30,34,35]. A complementary approach is to introduce heterogeneous architectures, such as gradient and multiphase structures, to exploit hetero-deformation-induced (HDI) stresses, which may enhance strain-hardening capacity and fracture resistance while retaining high strength [36,37].

Previous reviews have largely focused on a single processing route or alloy system, while discussions of the relationships among processing routes, defect evolution, microstructure, and service performance remain fragmented. In addition, although W and Mo are both Group 6 refractory metals and share many intrinsic characteristics, comprehensive comparisons of their similarities and differences remain limited. Accordingly, this review systematically examines W- and Mo-based refractory alloys and composites intended for extreme service conditions involving high temperatures, intense heat fluxes, irradiation, and high mechanical stresses, with particular emphasis on their strengthening and toughening mechanisms and irradiation resistance. The respective advantages and limitations of different processing routes are also discussed; homogeneous and heterogeneous microstructural design strategies are compared; and the effects of interfacial compatibility on properties, together with the underlying mechanisms of microstructural evolution under different thermodynamic and kinetic conditions, are analyzed from a microscopic perspective. This review aims to provide a mechanistic foundation for the rational design of cost-effective, high-performance refractory materials that can be fabricated into complex geometries. The resulting analytical framework may also provide guidance for the development of critical materials for strategic applications in aerospace and nuclear fusion.

2. Material design

Processing routes govern the thermodynamic and kinetic pathways through which compositional distributions, defects, and interfaces evolve, thereby linking materials design to macroscopic performance. Advances in processing now enable the controlled development of both homogeneous and heterogeneous microstructures. These architectures should be viewed as complementary design strategies, with their selection guided by the target combination of properties and service conditions.

2.1. Preparation method

The principal processing routes for W- and Mo-based refractory alloys and composites can be grouped into three categories: melting, AM, and PM. These routes are governed primarily by conventional melt solidification, rapid melting and solidification, and solid-state diffusion and sintering, respectively.

Melting processes represented by electron beam melting (EBM) [38], plasma arc melting (PAM) [39], and vacuum arc melting (VAM) combine purification with liquid-state solidification (Fig. 2(a–f)) [38–46]. Heat sources, atmospheres, temperature gradients, and cooling rates jointly determine impurity removal, elemental volatilization behavior, compositional uniformity, and the columnar-to-equiaxed grain transition. Detailed descriptions of the operating principles of these methods are provided in Supplementary Note S1. For the preparation of W/Mo materials, EBM generally provides the strongest purification capability, whereas PAM is more effective in suppressing elemental volatilization.

AM [47], commonly known as 3D printing [21,48,49], mainly uses laser or electron beams as energy sources [17,18,22,50]. For W/Mo materials, powder bed fusion (PBF) [19] and directed energy deposition (DED) [15,51] are representative AM routes for the near-net-shape

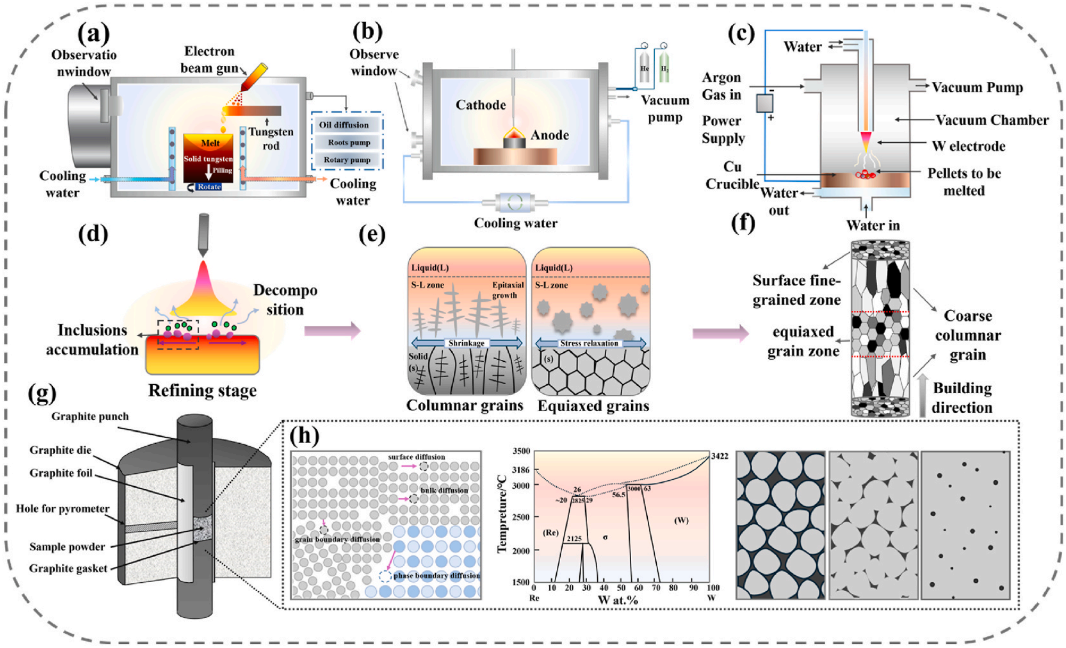

Fig. 2. (a–c) Schematic diagrams of the equipment for EBM, PAM, and VAM, respectively; (d) Purification and impurity removal mechanism of the melting process; (e) Schematic illustration of equiaxed grain growth; (f) Typical microstructure after solidification; (g) Schematic diagram of the sintering die for PM; (h) Sintering mechanism of PM, including atomic diffusion, solid-state phase transformation, and densification.

forming of complex components (detailed mechanisms are provided in Supplementary Note S2) [52]. Its rapid thermal cycling suppresses impurity migration and facilitates the formation of supersaturated solid solutions, ultrafine-grained (UFG) structures, and amorphous phases [53]. However, the high ductile-to-brittle transition temperatures (DBTTs), poor melt flowability, and fluctuating laser absorptivity of W and Mo can readily induce the balling effect and pore defects; the rapid heating and cooling cycles during AM further increase the cracking tendency [54]. Therefore, current studies mainly focus on crack suppression through process optimization and powder quality improvement [55,56]. Other AM techniques applicable to W/Mo materials include wire arc additive manufacturing (WAAM) [57] and binder jetting (BJ) [58], as summarized in Supplementary Note S3.

PM is one of the most widely used processing routes and generally comprises powder production, blending, compaction, sintering, and post-treatment [16,59,60]. As illustrated in Fig. 2(g and h), densification during PM is driven by the reduction of surface and interfacial energies and controlled by solid-state diffusion [61]. Powder production is a critical step in PM, because high-quality precursor powders are beneficial for obtaining fine and uniform grain structures during subsequent sintering. Common powder preparation methods for W- and Mo-based alloy powders include mechanical alloying (MA) [62], freeze-drying [63], wet-chemical synthesis [64], hydrothermal synthesis [65], and sol-gel processing [66], with detailed information provided in Supplementary Table S1. Common powder forming methods include die pressing, isostatic pressing, and powder injection molding (PIM) [67]. Sintering is the core step of PM. Conventional solid-state sintering and liquid-phase sintering (LPS) still play important roles, and LPS is particularly suitable for tungsten heavy alloys (WHAs) containing low-melting-point binder elements; however, prolonged heating can readily cause grain coarsening. In recent years, various advanced sintering techniques have attracted increasing attention [68,69]. Spark plasma sintering (SPS) [70], hot isostatic pressing (HIP) [71,72], and microwave sintering [73] provide more effective routes for improving densification and suppressing grain growth. In addition, emerging sintering processes such as oscillatory-pressure sintering [74] and ultrafast high-temperature sintering (UHS) [75] have also been developed, as detailed in Supplementary Note S4. Nevertheless, residual porosity remains a long-standing limitation of conventional PM. Residual pores can reduce electrical and thermal conductivity and may serve as crack initiation sites under certain loading conditions. Therefore, improving densification and controlling residual porosity remain central objectives in PM processing.

The operating principles, advantages, and limitations of the above preparation methods for W- and Mo-based materials are detailed in Supplementary Table S2. This comparison provides guidance for selecting an appropriate processing route according to the target properties and component geometries. Although the same three processing-route families are applicable to both metals, their relative priorities differ. Because W has a higher melting point and more pronounced low-temperature brittleness, full melting and fusion-based AM require particularly high energy input and stringent control of residual stress and cracking. Consequently, PM, liquid-phase-assisted densification in WHAs, and rapid or pressure-assisted sintering are especially prominent in W processing. Mo has a lower melting point and generally better room-temperature deformability, which can provide a comparatively broader window for melt-based fabrication and subsequent thermo-mechanical processing; nevertheless, oxygen contamination, porosity, columnar-grain formation, and cracking remain important concerns. Thus, W processing is often dominated by densification and crack suppression, whereas Mo processing more frequently requires a balance among impurity control, recrystallization, and formability [19,54,61].

In addition to these bulk-processing routes, physical vapor deposition (PVD) and chemical vapor deposition (CVD) provide surface-engineering approaches for preparing W- and Mo-based films and coatings. Such coatings offer localized protection, while multilayer or interlayer architectures can regulate interdiffusion and alleviate property mismatch at dissimilar-material interfaces. Ruset et al. [76] reviewed W coatings deposited on carbon-based substrates by vacuum plasma spraying (VPS), CVD, and PVD, showing that ion-assisted magnetron sputtering enables relatively thick W coatings with reduced delamination, while a Mo interlayer mitigates thermal-expansion mismatch. Kim et al. [77] further demonstrated that the thermal response of 5-μm PVD W/Mo coatings on graphite depends on coating architecture and heat load; the Mo interlayer improves adhesion, and the W/Mo bilayer exhibits better resistance to plasma heating. For

Mo-based coatings, Ahmed et al. [78] found that sputtering power and working-gas pressure jointly determine the crystallite size, porosity, roughness, and residual stress of direct-current (DC) magnetron-sputtered Mo films. High power combined with low-to-moderate pressure favors dense crystalline films, whereas increasing pressure changes the residual stress from compressive to tensile. Studies of other magnetron-sputtered coatings have also shown that service-induced elemental segregation and preferential oxidation can form an amorphous–crystalline surface layer that redistributes deformation and suppresses surface cracking [79], providing useful insights into the service evolution of W/Mo coatings. Nevertheless, practical applications remain constrained by intrinsic brittleness, deposition-induced residual stress, and interfacial degradation. Pure sputtered Mo films exhibit low crack-onset strain and straight channel cracks, although Re alloying can delay cracking within the solid-solution range [80]. Moreover, in W coatings with a Mo interlayer on carbon-fiber composite (CFC) substrates, carbon diffusion and carbide formation can degrade the CFC-Mo and Mo-W interfaces [77,81], while cyclic high-heat-flux loading may further induce nanopore formation and buckling delamination [82]. Therefore, deposition parameters, coating thickness, fracture resistance, interfacial reactions, and accumulated thermal cycles should be considered jointly when designing W/Mo protective coatings for long-term service.

2.2. Microstructure design

Microstructural designs in W- and Mo-based materials are classified here as homogeneous or heterogeneous. Homogeneous designs distribute solutes and second phases relatively uniformly to reduce local property variation, whereas heterogeneous designs deliberately combine regions differing in composition, phase constitution, grain size, or defect density to exploit interactions among them. The benefits of the latter depend on the mechanical integrity and thermal stability of the constituent regions and interfaces.

2.2.1. Homogeneous structure

Homogeneous design primarily relies on uniformly distributed substitutional solutes or thermally stable second-phase particles. The former provides solid-solution strengthening, whereas the latter contributes to grain refinement, dislocation pinning, and dispersion strengthening [23,83–85]. It should be noted that, because of the extremely high melting points of W and Mo and the demanding processing conditions they entail, second-phase particles are highly susceptible to agglomeration during fabrication. Such agglomeration may not only promote brittle-phase-induced cleavage fracture but also facilitate the formation of microstructural defects, thereby degrading material performance. Therefore, W- and Mo-based materials containing uniformly dispersed second phases are included in this section to emphasize the importance of controlling the spatial distribution of second-phase constituents.

Ti and Re [27], as well as Nb, V, and Ta [86], have been widely investigated for producing homogeneous solid solution microstructures in W- and Mo-based materials. As shown in Fig. 3(a and b), Zhang et al. [87] used laser powder bed fusion (L-PBF) to fabricate a crack-free Mo alloy containing a homogeneous Ti solid solution. Fig. 3(c and d) shows that Ti addition increases the average Taylor factor (TF) and promotes a more uniform distribution of geometrically necessary dislocation (GND) density, thereby reducing grain-to-grain deformation heterogeneity and mitigating local stress concentrations. Multielement alloying may further generate synergistic effects on phase stability and mechanical performance [88]. Liu et al. [89] used thermodynamic and empirical descriptors, including the enthalpy of mixing, entropy of mixing, Ω parameter, atomic size difference (δ), and valence electron concentration (VEC), to predict the phase constitution of W-Ta-Re alloys and evaluate their propensity to form detrimental phases. For an n-component alloy, these descriptors can be calculated as follows:

$$\Delta H_{mix} = \sum_{i=1, i\neq j}^{n} \Omega_{ij} c_i c_j \quad (1)$$

$$\Delta S_{mix} = -R \sum_{i=1}^{n} (c_i \ln c_i) \quad (2)$$

$$\Omega = \frac{T_m \Delta S_{mix}}{|\Delta H_{mix}|}, T_m = \sum_{i=1}^{n} c_i (T_m)_i \quad (3)$$

$$\delta = \sqrt{\sum_{i=1}^{n} c_i \left(1 - \frac{r_i}{\bar{r}}\right)^2}, \bar{r} = \sum_{i=1}^{n} c_i r_i \quad (4)$$

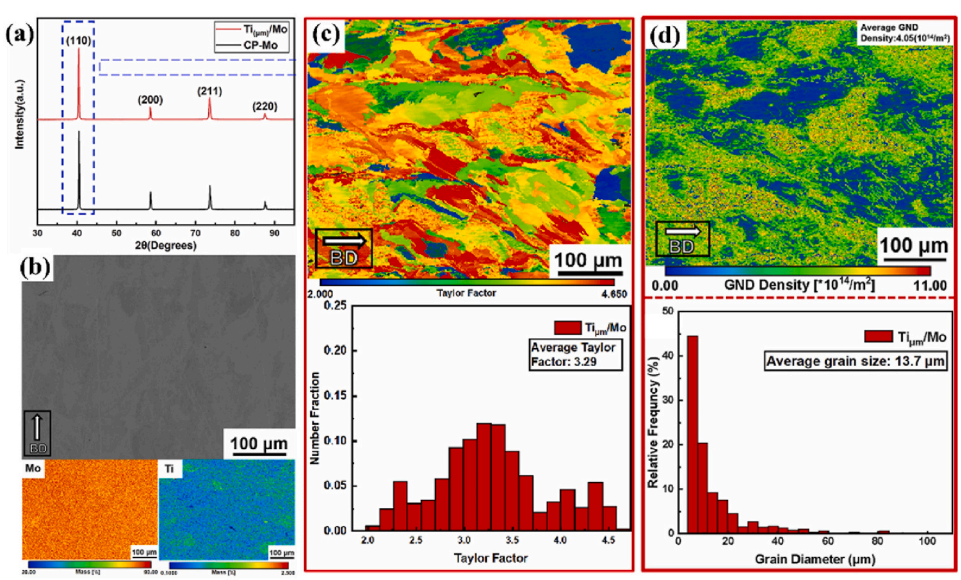

Fig. 3. (Reprinted from Ref. [87]) (a) X-ray diffraction patterns of L-PBF fabricated commercially pure Mo (CP-Mo) and $Ti_{\mu m}$/Mo alloy; $Ti_{\mu m}$/Mo alloy fabricated by L-PBF: (b) scanning electron microscopy (SEM) image and electron probe microanalysis (EPMA) elemental maps; (c) TF distribution maps and corresponding distribution curves; (d) GND distribution maps and grain size distribution diagrams.

$$VEC = \sum_{i=1}^{n} c_i (VEC)_i \quad (5)$$

where n is the number of components; c_i is the atomic fraction of element i; Ω_{ij} is the pairwise interaction parameter between elements i and j; and R, T_{mi}, r_i, and $(VEC)_i$ are the gas constant, melting point, atomic radius, and valence electron concentration of element i, respectively. The Ω parameter compares the entropy-stabilizing contribution with the enthalpy of mixing, δ quantifies the overall atomic-size mismatch, and VEC is commonly used to estimate the preferred crystal structure. A smaller δ generally favors single-phase solid-solution formation, while VEC < 6.87 has been empirically associated with BCC solid solutions. These composition-based descriptors are intended for preliminary screening and should be interpreted as empirical tendencies rather than universal phase-selection rules.

Alloying element content is another key variable in homogeneous microstructural design. Yang et al. [90] reported that, in Mo-10B alloys, B in excess of its solid solubility limit precipitated as Mo_2B, while pores occupied approximately one-third of the observed surface area. Optimization of the processing route can also promote the formation of homogeneous microstructures. Conklin et al. [91] treated W powder with perrhenic acid ($HReO_4$) through sequential wetting, drying, and reduction steps. This treatment produced a continuous Re-containing coating on the W particles and promoted prealloying. A χ phase interlayer containing 71–75 at.% Re formed, reducing the diffusion distance of Re during sintering and thereby promoting the formation of a homogeneous single-phase solid solution.

For homogeneous microstructures strengthened by second-phase dispersion, conventional solid-state mixing often produces nonuniform particle distributions. Liquid-phase synthesis routes have therefore been widely adopted to improve particle dispersion [92], as described in Supplementary Note S5. Xiao et al. [93] combined liquid-phase doping with hydrothermal treatment to mix Zr^{4+} and Y^{3+} uniformly with a W precursor at the molecular scale. Following HIP consolidation, $Zr(Y)O_2$ nanoparticles were uniformly dispersed throughout the alloy. Yang et al. [94] used solution combustion synthesis (SCS) to obtain a uniform distribution of La_2O_3 particles measuring 10–50 nm within grains and 50–500 nm along grain boundaries, even at a relatively high La_2O_3 content of 5.0 wt%. At high sintering temperatures, however, enhanced diffusion and the thermodynamic tendency to reduce interfacial energy can drive second-phase particles toward grain boundaries. Core-shell powder design [95–97] and in situ precipitation can instead control diffusion distances and nucleation sites, thereby improving particle dispersion. Further details are provided in Supplementary Note S6. Lang et al. [98] synthesized core-shell precursors comprising a TiC core and a tungstic acid shell using a modified wet-chemical method. This architecture suppressed TiC agglomeration and promoted a relatively uniform intragranular distribution of TiC particles within the W matrix. Hu et al. [99] used thermal plasma synthesis to dissolve Y_2O_3 rapidly within the NC W lattice, thereby forming a metastable solid solution. Subsequent sintering at 1600 °C induced the uniform intragranular precipitation of Y_2O_3 particles with an average size of approximately 970 nm. In addition, tailoring the crystallographic orientation relationship between the precipitates and matrix can reduce interfacial energy and suppress particle agglomeration [100,101]. As discussed in Section 3.2, such interface engineering can further support the development of homogeneous microstructures.

Collectively, these studies show that uniformity alone is insufficient because particle size distribution and interface chemistry independently affect material properties. However, homogeneity is still assessed mainly from as-sintered microstructures. Because metastable intragranular precipitates may redistribute or coarsen during subsequent forming and long-term service, microstructural observations should be accompanied by volume-representative dispersion statistics and high-temperature stability data.

2.2.2. Heterogeneous structure

Heterogeneous structures [102–104] can generate HDI stresses during deformation [105,106], which arise from deformation incompatibility between relatively soft and hard domains. This incompatibility promotes the accumulation of geometrically necessary dislocations near domain boundaries, producing back stress in the soft domains and forward stress in the hard domains. These coupled stresses enhance strain hardening and load sharing, although the resulting mechanical benefit depends on domain contrast, interfacial integrity, and structural stability. Representative W- and Mo-based architectures include multimodal [107], multilayer [108,109], and gradient structures.

Recent studies have advanced heterogeneous structure design. Ning et al. [107] produced heterostructured pure W comprising elongated grains with numerous low-angle grain boundaries and blocky recrystallized grains. The coexistence of transgranular cracking in elongated grains and intergranular cracking in recrystallized regions increased crack path tortuosity and the total work of fracture. This mechanism differs from homogeneous grain refinement, in which strengthening arises mainly from uniformly distributed grain boundaries. Li et al. [110] developed bimodal and lamellar structures in a W-Y_2O_3 alloy, yielding a tensile strength of approximately 1.0 GPa and an elongation of 26% at 200 °C. This property combination suggests strength-ductility synergy under the reported test conditions. Hu et al. [111] prepared the WTaTiVN + $Ta_{\mu m}$ heterostructured alloy shown in Fig. 4(a and b). Fig. 4 (c–f) shows three regions: Ta islands, high-entropy alloy (HEA) islands, and an HEA matrix. Coarse-grained (CG; >5 μm), fine-grained (FG; 1–5 μm), and ultrafine-grained (UFG; <1 μm) regions form a multimodal structure. Regional hardness differences may contribute to HDI strengthening. Awasthi et al. [112] fabricated a multiphase W-Nb-C alloy using L-PBF. Phase contrasts in elastic modulus and yield strength were associated with HDI strengthening; for example, NbC and the W-Nb solid solution had elastic moduli of 535 and 400 GPa, respectively. In Mo-based materials, heterogeneous structures are used mainly for functional integration [113]; their application under extreme conditions remains less studied than in W-based materials. Ren et al. [114] found that, in a Mo-containing dual-phase alloy, controlled partial recrystallization generated a deformable recrystallized phase within a continuous skeleton of the unrecrystallized hard phase, thereby coordinating strain and redistributing stress while suppressing interfacial cracking. This finding indicates that the spatial continuity and microstructural state of individual regions are also critical. These cases show that multimodal and multiphase designs can provide the mechanical contrast needed for HDI strengthening. Nevertheless, tensile ductility, fracture toughness, crack growth resistance, and microstructural stability at relevant service temperatures should be evaluated jointly.

Gradient structures reduce abrupt thermophysical and mechanical mismatches and are therefore attractive for Mo-based materials under severe thermal gradients [115,116]. For example, AlN/Mo functionally graded materials use a gradual ceramic-to-metal transition to relieve thermal stresses caused by steep temperature gradients and thermophysical mismatch. The Wakashima power law commonly controls this transition, with exponent p defining the gradient profile [117], and can be expressed as follows:

$$C_{Mo} = K \cdot \left(\frac{x}{d}\right)^p \quad (6)$$

where C_{Mo} is the mass fraction of Mo in a given gradient layer, x is the layer position, d is the total thickness of the gradient layer, K is a constant related to the density of the raw materials, and p is the compositional exponent. Jia et al. [118] showed that ceramic interlayer strength and p govern crack propagation, whereas strength differences between adjacent layers determine crack initiation sites. This function-based approach may also guide phase distribution control in W-based graded composites for extreme environments.

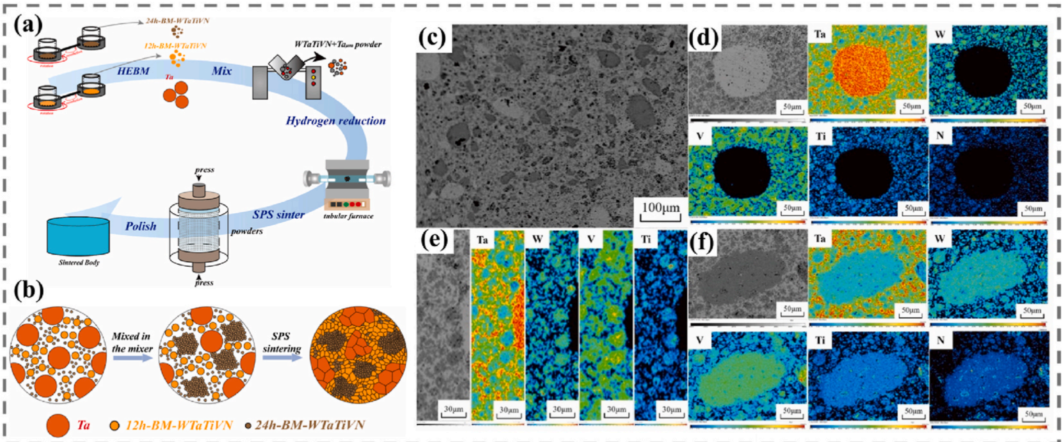

Fig. 4. (Reprinted from Ref. [111]) (a) Schematic diagram of the heterogeneous WTaTiVN + $Ta_{\mu m}$ manufacturing process; (b) Rearrangement of powders and generation of three-phase heterostructures in WTaTiVN + $Ta_{\mu m}$.(c) backscattered electron (BSE) image of WTaTiVN + $Ta_{\mu m}$ and (d–f) elemental color maps of Ta, W, Ti, V, and N in light-colored islands, and matrix and dark-colored islands.

In W-based composites, gradient designs are used mainly in WHAs [119] and W-Cu composites [120,121]. Relevant applications are summarized in Supplementary Note S7. Deng et al. [122] prepared W@NiFe composite powders by intermittent electrodeposition. Following LPS at 1470 °C for 0.5 or 1 h, the alloy developed a mechanical property gradient along the gravity direction, consistent with the hard-surface and tough-core requirements of armor-piercing cores. Zhang et al. [123] used low-cost gray cast iron as a solid-state carbon source to reinforce W-Cu graded materials through in situ WC formation. After hot-press sintering, a WC + Cu layer, an Fe_3W_3C + W(Fe) + Cu transition layer, and the original W + Cu region formed along the C/Fe diffusion direction. This architecture improved interfacial bonding and reduced particle detachment risk, a common problem in composites reinforced with externally added ceramics. These studies show that gradient structures can spatially integrate functions while avoiding abrupt property changes. However, effective crack suppression also requires control of reaction products, phase continuity, and local porosity, not merely smooth compositional gradients.

Overall, homogeneous and heterogeneous designs address different limitations of W- and Mo-based materials. Homogeneous solid solutions and particle dispersions generally provide isotropic strengthening, stable load transfer, and good processing reproducibility but may offer less strain hardening and crack deflection. Heterogeneous structures can improve strain accommodation and fracture resistance through HDI stresses, crack deflection, and spatial functional integration but are more sensitive to interfacial integrity, property contrast, and microstructural stability. Therefore, heterogeneous structures should not be considered universally superior to homogeneous structures. A promising route is to combine both strategies by stabilizing heterogeneous regions with uniformly dispersed nanoscale phases, thereby coupling local stability with macroscopic strain partitioning. It has been reported that a high density of uniformly distributed nanoprecipitates formed within a BCC matrix, with a lattice misfit of only approximately 0.37%. Interactions between the precipitates and dislocations provided precipitation strengthening, while their uniform distribution helped retain tensile ductility. Combined with the coexistence of mechanically dissimilar soft and hard regions, this multiscale heterogeneous architecture achieved a favorable strength–ductility balance [124].

3. Microstructure tailoring

3.1. Thermodynamic driving forces and kinetic control of microstructural evolution

Microstructural features, including grain morphology and size, phase constitution and distribution, and crystal defects, evolve with the thermodynamic state and processing history. Such evolution directly affects macroscopic properties. Understanding these changes is therefore essential for property optimization. Pure W is difficult to process because of its high melting point and poor room-temperature ductility [29]. Low-melting-point elements such as Ni, Fe, and Cu are therefore added to produce WHAs with a typical two-phase composite microstructure [125,126]. WHAs undergo complex microstructural evolution during processing, hot working, and service and are therefore widely studied as representative W-based systems. WHA evolution is commonly described by dissolution-reprecipitation [127] and Ostwald ripening [128,129]. Dihedral angle and W-W contiguity are key indicators of this evolution [126] (Supplementary Equations S1–S2). By contrast, many Mo alloys retain a continuous BCC matrix and undergo more extensive thermomechanical deformation; solute redistribution, precipitate stability, dislocation substructures, recovery, and recrystallization are therefore more frequently used to interpret their evolution. Fundamentally, microstructural evolution reflects the interplay between thermodynamic driving forces and kinetic constraints [130,131]. Thermodynamic driving forces determine whether microstructural evolution is energetically feasible, whereas kinetic factors control its pathway, rate, and ultimate attainable extent. Accordingly, this section first examines common modes of microstructural evolution driven by deformation-induced stored energy and reductions in chemical free energy, and then discusses how deformation and thermal kinetics govern the resulting microstructures.

By introducing abundant crystal defects, plastic deformation stores strain energy that provides a major thermodynamic driving force for subsequent microstructural evolution. Under thermal activation, this energy is dissipated through dynamic recovery (DRV) and dynamic recrystallization (DRX) [132]. Re addition can modify dislocation behavior and recrystallization. Huang et al. [133] observed deformation twin bands in Mo-47.5Re during room-temperature compression, which they attributed to limited thermal activation. At elevated temperatures, DRV became the primary energy dissipation mechanism. By comparison, Ma et al. [134] found that, during room-temperature tension of Mo-14Re, strain energy accumulated mainly in slip-induced dislocation cells and networks, increasing lattice distortion. The stored strain energy provided an additional driving force for DRX at elevated temperatures. The differences between these studies likely reflect both Re content and loading mode. A high Re content can reduce stacking fault energy and raise the recrystallization temperature, promoting twinning at room temperature. Lower-Re alloys exhibit weaker solid-solution strengthening and solute pinning, which can facilitate DRX nucleation and growth. Together with loading mode effects, weaker solute pinning may make lower-Re alloys more susceptible to DRX, although temperature, strain rate, and accumulated strain must also be considered.

In addition to deformation-induced stored energy, reductions in chemical free energy constitute another major thermodynamic driving force for microstructural evolution. Reactive alloying and tailored heat treatments can lower system free energy through chemical reactions [135] or thermally activated solute redistribution. Yang et al. [136] added Ti_3AlC_2 (a MAX phase) to Mo alloys; sintering at 1960 °C induced a topochemical reaction that formed stable $AlTi_3$ and Ti-O Magnéli phases. This reaction dissipated stored energy and thereby suppressed recrystallization. Calculations by Yang et al. [137] indicated that B could form a stable solid solution in the Mo matrix, with $\Omega > 1$ suggesting entropy-favored mixing. B atoms also exerted a strong solute drag effect that impeded grain boundary migration. Li et al. [138] reported that reactive Zr scavenged O from pre-existing titanium oxides in low-oxygen titanium-zirconium-molybdenum (TZM) alloys at high temperatures. Ti remained dissolved in the Mo matrix, forming a high-energy metastable supersaturated solid solution. Subsequent water quenching created substantial undercooling, while rolling introduced a high vacancy density. Together, these factors promoted the uniform precipitation of Ti-rich nanophases. These examples also show that thermodynamic favorability alone does not determine the final microstructure; the extent of reaction, solute redistribution, and precipitation depends on the available time for atomic diffusion and grain-boundary migration.

The role of kinetic control is particularly evident in the strong temperature dependence of plastic deformation and the associated accumulation and dissipation of stored energy. At low temperatures, plastic flow in BCC W and Mo is constrained by the limited mobility of $1/2\langle 111\rangle$ screw dislocations, whose nonplanar cores and high lattice friction make their glide reliant on thermally activated kink-pair nucleation [84,139,140]. Insufficient thermal activation therefore increases the flow stress and may promote cleavage or intergranular fracture before extensive plastic deformation can develop. This constraint is generally more pronounced in W because of its higher DBTT, whereas Mo usually retains a comparatively broader low-temperature deformation window. Alloying and particle/interface design can partly alleviate this limitation by promoting dislocation nucleation and slip or improving grain-boundary cohesion. As temperature increases, enhanced screw-dislocation mobility and the activation of cross-slip and climb facilitate more homogeneous plastic flow and DRV; under sufficiently large strains, the accumulated energy may also drive DRX [132,134]. However, improved thermally activated plasticity may be offset by particle coarsening, grain growth, or recrystallization-induced grain-boundary weakening [100,141]. Comparisons between W- and Mo-based materials should therefore consider homologous rather than absolute temperature and account for strain rate, loading mode, grain size, texture, impurity content, and recrystallization state.

Under extreme processing conditions, materials can be driven far from thermodynamic equilibrium, making kinetic constraints central to microstructural evolution. Under large strains at elevated temperatures, rotational dynamic recrystallization (RDRX) can become an important softening mechanism in W- and Mo-based alloys. RDRX involves subgrain rotation and the progressive conversion of low-angle grain boundaries (LAGBs) into high-angle grain boundaries (HAGBs). Its characteristic timescale can be estimated using the subgrain rotation time equation. Thermally activated deformation kinetics are commonly described using the Arrhenius-type constitutive equation and the Zener-Hollomon parameter [125,132,136]. The corresponding equations and parameters are provided in Supplementary Equations S3–S5.

Under high-strain-rate impact or severe shear, dislocation density increases rapidly, and much of the plastic work is converted into heat over a short timescale. This thermomechanical coupling can produce ultrafine-grained or NC structures. Zhang et al. [125] investigated the microstructural evolution of a 90W-Ni-Fe alloy under high-strain-rate deformation using a split Hopkinson pressure bar (SHPB). As shown in Fig. 5(a), dislocation tangles, cells, and subgrains formed sequentially below 4779 s^{-1}, whereas a 50-μm-wide adiabatic shear band developed at 6146 s^{-1} (Fig. 5(b–i)). The authors attributed the fine equiaxed grains within the shear band to RDRX: increasing strain and temperature transformed dislocation structures into elongated subgrains, which rotated and ultimately formed randomly oriented equiaxed grains. Zhou

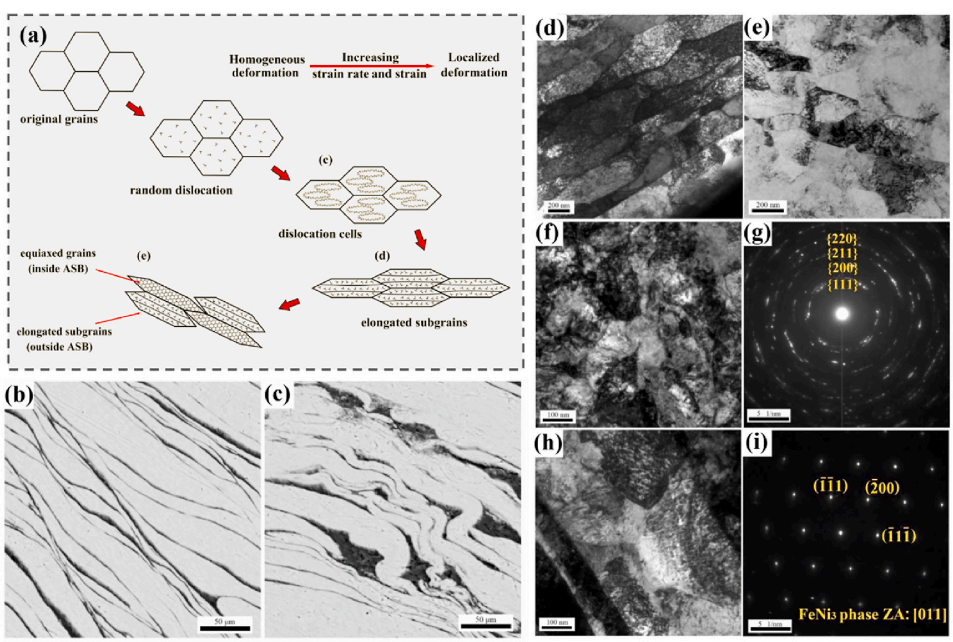

Fig. 5. (Reprinted from Ref. [125]) (a) Schematic diagram of microstructural evolution of 90W-Ni-Fe alloy under high-strain-rate deformation; SEM images of the microstructure inside the adiabatic shear band (ASB): (b) Severely elongated tungsten particles; (c) Rotation of tungsten particles. Transmission electron microscopy (TEM) images of 90W-Ni-Fe alloy at a strain rate of 6146 s^{-1}: outside the shear band: (d) Numerous lath-shaped subgrains in the tungsten phase; (e) Elongated subgrains in the γ-(Ni, Fe) solid solution phase; inside the shear band: (f) and (h) Fine equiaxed grains in tungsten phase and γ-(Ni, Fe) phase, respectively; (g) and (i) Selected-area electron diffraction (SAED) patterns corresponding to panels (f) and (h), respectively.

et al. [142] examined adiabatic shear failure in a 93W-4.9Ni-2.1Fe alloy at 6000 s^{-1}. Thermoplastic instability first caused shear localization, followed by DRX as the adiabatic temperature reached 1565 K; at 70% strain, stress concentrations at recrystallized grain boundaries promoted microvoid nucleation, coalescence, and cracking along W/γ-(Ni,Fe) interfaces. Wang et al. [143] applied high-pressure torsion (HPT) at 400 °C and 1.5 GPa to Ta-modified WHAs, imposing severe shear and inducing continuous dynamic recrystallization. In the 18 wt% Ta alloy, W grains refined to approximately 2.20 μm after 15 revolutions, Ta grain sizes remained at 2.07–2.63 μm, and DRX produced ultrafine γ grains with an HAGB fraction of 90.2%. Together, these studies show that increasing strain rate accelerates defect storage and reduces the time available for recovery, whereas adiabatic heating can locally restore atomic mobility and promote RDRX. The competition between these processes determines whether grain refinement or shear localization and failure dominate.

In addition to deformation kinetics, heating and cooling rates regulate diffusion kinetics. Rapid thermal cycling and steep temperature gradients limit the time available for long-range atomic diffusion, preserving nonequilibrium microstructures at room temperature [144,145]. Hao et al. [146] prepared a WHA by laser-directed energy deposition (L-DED), in which steep melt pool temperature gradients and drag forces from liquid flow drove W particle migration, producing alternating W-particle-rich, W-dendritic, and W-particle-poor layers. Zhou et al. [147] prepared a ZrO_2-reinforced WHA by SPS. The heating rate of 100 °C/min limited atomic diffusion and grain growth, while ZrO_2 particles further suppressed W grain coarsening. After sintering at 1250 °C for 10 min, the W grain size remained 1.51 μm. Dai et al. [148] investigated a W-5Ni-2Cu alloy quenched from 1000 to 1200 °C. As W solubility in the γ phase increases with temperature, rapid cooling suppresses long-range diffusion, retains the high-temperature W solid solution at room temperature, and inhibits intermetallic formation and impurity segregation at grain boundaries. Overall, thermodynamic driving forces define the energetically favorable direction of microstructural evolution, whereas kinetic conditions determine its pathway, rate, and attainable extent. Their coupling explains why W- and Mo-based materials with similar compositions may develop different grain structures, phase distributions, and defect populations under distinct deformation and thermal histories.

3.2. Interfacial bonding mechanisms

Interfaces govern load transfer, crack arrest, and stress redistribution. Weak interfaces may debond before effective load transfer, whereas excessively strong interfaces may direct cracks into brittle constituents and suppress energy-dissipating pull-out or deflection. Therefore, understanding interfacial bonding mechanisms is essential [149]. Nevertheless, W- and Mo-based materials still face interfacial challenges. In second-phase-reinforced systems, externally introduced phases may exhibit substantial lattice mismatch with the matrix [150]. In dissimilar systems such as W-Cu, immiscibility limits metallurgical bonding, while thermal expansion mismatch promotes interfacial stress and cracking [59,151]. Current studies classify interfacial bonding in W- and Mo-based alloys and composites as diffusion bonding, reaction-induced bonding, or lattice-matching-induced coherent or semi-coherent bonding.

At high temperatures, interdiffusion between W/Mo and adjoining constituents forms a compositionally graded transition layer and metallurgical bonds. However, atomic diffusion also contributes to most interfacial bonding processes. Both W and Ta have BCC structures and similar atomic radii and electronic configurations. Their interfacial bonding is therefore governed mainly by interdiffusion and substitutional solid solution formation. Xu et al. [152] prepared W/Ta laminated composites by SPS. Extensive W-Ta interdiffusion formed a 3-μm-thick diffusion zone and a continuous substitutional solid solution region, which helped relieve interfacial stress during thermal shock. Because W and Cu exhibit negligible interdiffusion under conventional conditions, Xu et al. [151] introduced a CrCoNi medium-entropy alloy (MEA) interlayer to improve bonding in oxide dispersion strengthened W (ODS-W)/Cu joints. At the ODS-W/MEA interface, interdiffusion among W, Cr, Co, and Ni formed a supersaturated solid solution and an amorphous diffusion layer (Fig. 6(a–d)). Cu-MEA interdiffusion also produced a supersaturated solid solution at the Cu/MEA interface (Fig. 6(e–h)). Nanoscale Cu-rich and Cr-rich phases precipitated during cooling, contributing to solid solution and precipitation strengthening. After SPS at 1000 °C, the joint tensile strength increased by 171% relative to that of the directly diffusion-bonded joint.

In composites, lattice continuity across the reinforcement-matrix interface is critical for interfacial stability and load transfer. Interfaces are classified as coherent, semi-coherent, or incoherent according to the lattice mismatch (δ). When $\delta < 5\%$, an interface is generally considered coherent, with continuous and closely matched lattices across the interface. Such interfaces usually have low interfacial energy but can retain elastic coherency strain. When $5\% < \delta < 25\%$, a semi-coherent interface commonly forms, and periodically distributed misfit dislocations partly relax the mismatch while preserving regions of lattice continuity. When $\delta > 25\%$, the interface is generally considered incoherent and exhibits discontinuous atomic matching and higher interfacial energy. Owing to favorable lattice matching, coherent and semi-coherent interfaces generally exhibit low interfacial energy and high work of separation, thereby resisting interfacial debonding and cracking under loading [153,154]. Hu et al. [155] identified several low-mismatch

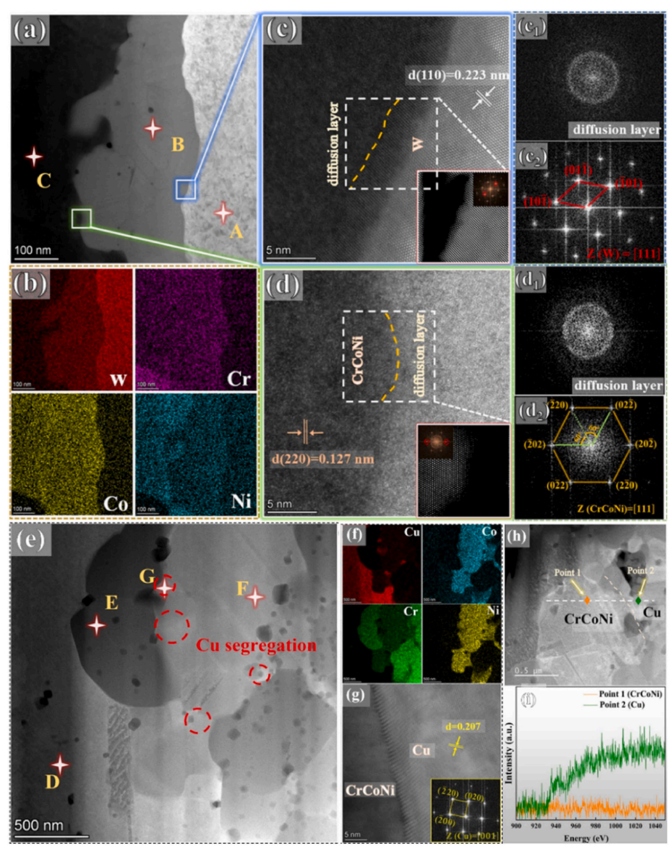

Fig. 6. (Reprinted from Ref. [151]) (a) TEM images of ODS-W/MEA interface prepared at 1000 °C; (b) Elemental distributions of W, Cr, Co, and Ni at the interface; (c, c1, c2) high-resolution transmission electron microscopy (HRTEM) image of the W/diffusion layer interface and the fast Fourier transform (FFT) images; (d, d1, d2) HRTEM image of the MEA/diffusion layer interface and the FFT images. MEA/Cu interface prepared at 1000 °C: (e) TEM image, (f) Elemental distributions of Cu, Cr, Co, and Ni, (g) HRTEM image, (h, i) electron energy-loss spectroscopy (EELS) analysis at the MEA/Cu interface.

coherent interfaces in TiC-doped Mo alloys: $(1\,\overline{2}\,1)$ TiO_2//(110) Mo(δ = 2.6%), $(\overline{1}\,211)$ Ti_8O_{15}//(110) Mo(δ = 1.4%). These interfaces promoted a transition from intergranular to transgranular quasi-cleavage fracture. Semi-coherent interfaces can also facilitate stress and plastic strain transfer. Li et al. [156] fabricated a TZM alloy containing crown-like composite second phases composed of TiO_2 cores partially coated with ZrO_2. TiO_2 formed a semi-coherent interface with the Mo matrix at 8.70% mismatch, whereas ZrO_2 formed an incoherent interface. The attachment of ZrO_2 to TiO_2 improved interfacial bonding and reduced susceptibility to microcrack initiation. Fan et al. [157] prepared a W-Al_2O_3 alloy containing coherent and semi-coherent interfaces. These interfaces promoted crack penetration through Al_2O_3 particles along W grain boundaries, increasing energy dissipation during crack propagation. Their low interfacial energy may also limit the agglomeration and coarsening of second-phase particles. Xie et al. [158] found that the semi-coherent TiC/W interface in a W-0.5 wt% TiC alloy had an interfacial energy of 1.23 J/m^2 and a work of separation of 8.56 J/m^2. The TiC particles thus retained an average size of 29 nm and a uniform distribution after high-temperature sintering and forging. Notably, the resulting coherent or semi-coherent interface depends on alloying content, which therefore requires careful optimization [159]. These interfaces may also improve the irradiation resistance of W- and Mo-based alloys and composites in fusion environments [150,160], as discussed in Section 5.

Chemical strengthening arises from interfacial bond formation or new phases generated by in situ reactions. Interfacial bond formation redistributes valence electrons through charge transfer or sharing, thereby increasing cohesion. Covalent bond-forming reactions, characterized by high bond energy and directionality, can improve wettability and bonding between reinforcing phases and matrices. At Mo grain boundaries, segregated O draws charge from neighboring atoms, increases ionic character, weakens metallic bonding, and reduces cohesion [100]. Ji et al. [161] found that TiC nanoparticles reacted in situ with O impurities at Mo grain boundaries during SPS, forming Ti_3O_5 nanoparticles. As shown in Fig. 7, first-principles calculations revealed substantial charge transfer at Mo grain boundaries and Ti_3O_5/Mo interfaces because of electronegativity differences among Mo, Ti, and O. Charge accumulated among Mo, Ti, and O, forming Mo-Ti-O covalent bonds stronger than Mo-Mo bonds. The Mo-Ti_3O_5 composite consequently exhibited a compressive yield strength of 1340 MPa and a fracture strain above 50%. Metallic bonds are nondirectional and delocalized, allowing interfacial deformation compatibility while improving strength [162]. Wang et al. [163] formed orthorhombic Ni_3Ta nanophases in situ in a W-Ni_3Ta alloy. The nanophases shared Ni atoms with γ-(Ni,Fe), producing continuous Ta-Ni metallic bonding across the interface. This

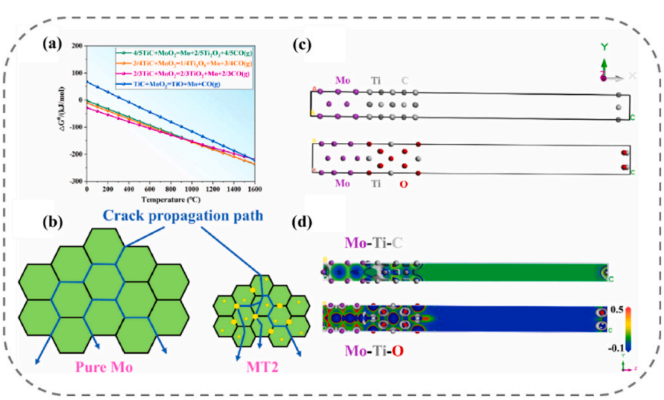

Fig. 7. (Reprinted from Ref. [161]) (a) Gibbs free energy change plots revealing the thermodynamic feasibility of oxidation reactions; (b) schematic diagram of crack propagation path in pure Mo and MT2; (c) modeling of the Mo/TiC and Mo/Ti_3O_5 interfaces in different configurations; (d) the electron localization function of (c).

bonding promoted coordinated interfacial deformation, yielding a tensile strength of approximately 1140 MPa and an elongation of 14.8%. Interfacial chemical bonding is commonly introduced through in situ reactions [164], which form intermetallic compounds or solid solutions bridging the matrix and second phase [165]. These products form strong interfacial bonds [162,163] and may reduce interfacial energy through lattice matching, thereby acting as transition layers between the matrix and reinforcing phase. Mao et al. [165] introduced trace O_2 during SPS to form nanosized Al_2O_3 and t-ZrO_2 particles in situ in W alloys. Al_2O_3 was partly distributed between W grains and the binder phase, forming a rivet-like interlocking structure, whereas t-ZrO_2 formed a semi-coherent interface with the W matrix. Together, these in situ reactions produced a dense, well-bonded interfacial structure.

Advances in computational materials science, particularly first-principles calculations, have enabled deeper understanding of interfacial bonding at the atomic and electronic scales [100,161]. Computational methods may therefore guide interface design and reduce trial-and-error costs by predicting interfacial strength and its effects on mechanical properties [34,166]. Nevertheless, parameters derived from idealized interface models do not directly determine macroscopic fracture resistance, because real interfaces contain various defects and their failure behavior also depends on interface architecture and the local stress state. Studies of other composite systems have shown that interface architecture can modify local stress triaxiality and redirect failure from cavitation-dominated cracking toward distributed shear deformation and local necking [167]. Therefore, interface design for W/Mo composites should integrate computational predictions with experimental characterization and consider interface geometry, spacing, stress-state regulation, and service conditions rather than pursuing maximum theoretical strength alone.

4. Strengthening and toughening mechanisms

Strengthening and toughening strategies for W and Mo materials aim to improve their room-temperature ductility and toughness, high-temperature creep resistance, and irradiation resistance without sacrificing strength or hardness [45]. Within the framework of defect engineering, these property improvements rely on the rational control of the types, densities, and distributions of crystal defects. Depending on their characteristic length scales, stability, and service conditions, different defects may produce strengthening by impeding dislocation motion or improve ductility and toughness by facilitating strain accommodation and energy dissipation; meanwhile, competing effects may also arise.

Fig. 8(a) presents a room-temperature ultimate tensile strength (UTS)–total elongation map compiled from relevant strengthening and toughening studies cited in this section. For reference, the reported room-temperature tensile strengths of pure W and Mo typically range from 400 to 700 MPa, and both exhibit room-temperature brittleness. As shown in the figure, some materials achieve elongations of approximately 40% while maintaining UTS values close to 1.0 GPa, indicating that strength-ductility synergy can be achieved through appropriate compositional and processing designs. Nevertheless, the dataset as a whole still exhibits the general trend that an increase in elongation is accompanied by a decrease in strength. Because grain-size data are more abundant and straightforward for W-based systems, Fig. 8(b) focuses primarily on these materials. Tungsten heavy alloys generally exhibit relatively coarse grains, whereas carbide- or oxide-reinforced systems and W-Re-Ta alloys possess finer grains. These differences may result from the combined effects of ductile binder phases, solute additions, and particle pinning. To explore the mechanisms underlying these variations in properties and microstructures, this chapter classifies the strengthening and toughening mechanisms according to defect type. Fig. 8(c–f) illustrates the four most common mechanisms: solid-solution strengthening, grain-refinement strengthening and toughening, second-phase strengthening, and dislocation strengthening. It should be noted that Fig. 8(a and b) provides an overall view of the reported property

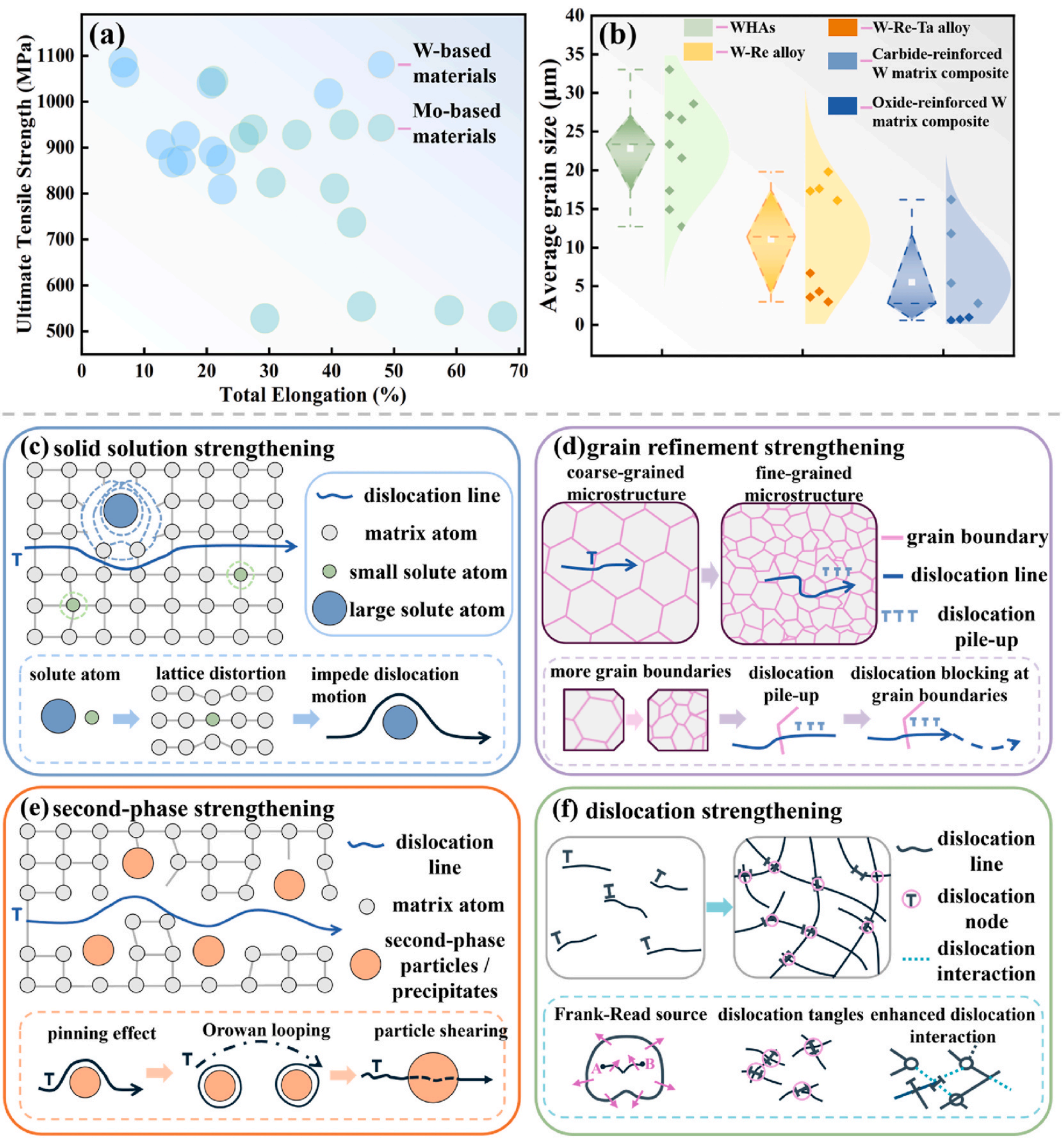

Fig. 8. (a) Relationship between room-temperature ultimate tensile strength (UTS) and total elongation of W- and Mo-based materials. Marker sizes are used solely for visualization. Owing to differences in testing conditions and material histories among the source studies, the data are intended to show overall property distributions rather than enable direct quantitative ranking. (b) Average grain-size distributions of representative W-based material classes. Schematic illustrations of (c) solid-solution strengthening, (d) grain-refinement strengthening and toughening, (e) second-phase strengthening, and (f) dislocation strengthening. Complete data sources and the corresponding processing and testing conditions are provided in Supplementary Tables S3 and S4.

distributions rather than a basis for direct quantitative ranking, because specimen dimensions, strain rates, and prior thermomechanical histories differ among the source studies. Detailed testing conditions for the individual data points are provided in Supplementary Tables S3 and S4.

4.1. Point defect construction

Solid-solution strengthening arises from elastic interactions between the strain fields of solute atoms and dislocations, which impede dislocation motion and increase strength and hardness. For multicomponent W/Mo alloys, the root-mean-square superposition model is commonly used to estimate the overall solid-solution strengthening contribution [129], whereas Fleischer or Labusch models are applied to single-solute systems [137]. The former combines individual solute contributions, whereas the latter relate strengthening to solute-dislocation interactions. The corresponding equations and parameters are provided in Supplementary Equations S6–S7.

Solid-solution strengthening often reduces ductility, whereas the Re effect can increase strength, lower the DBTT, and improve low-temperature ductility. Proposed mechanisms include enhanced dislocation cross-slip, altered grain boundary segregation, and electronic structure modification upon Re dissolution [27], as detailed in Supplementary Note S8. The Re effect depends strongly on Re content and temperature [139,140]. In Mo-Re alloys, 5–17 wt% Re has been associated with peak ductility, whereas contents above 40 wt% provide stronger strengthening. In W-Re alloys, limiting Re to 1–26 wt% reduces the risk of brittle W_2Re_3 formation. Zhang et al. [168] investigated W-xRe alloys (x = 0, 3, 5, and 10 wt%) and found that Re promoted dislocation slip and improved toughness at 50–200 °C. At 150 °C, long, straight surface slip steps formed, and their density increased with Re content (Fig. 9(a–h)). Above 300 °C, Re–dislocation interactions generated jogs and loops that impeded dislocation motion and potentially increased the DBTT(Fig. 9(i–l)). Compared with pure W, W-10Re exhibited stronger defect interactions, with pinning intensifying as temperature and defect density increased. This solid solution softening-to-hardening transition highlights the need to optimize Re

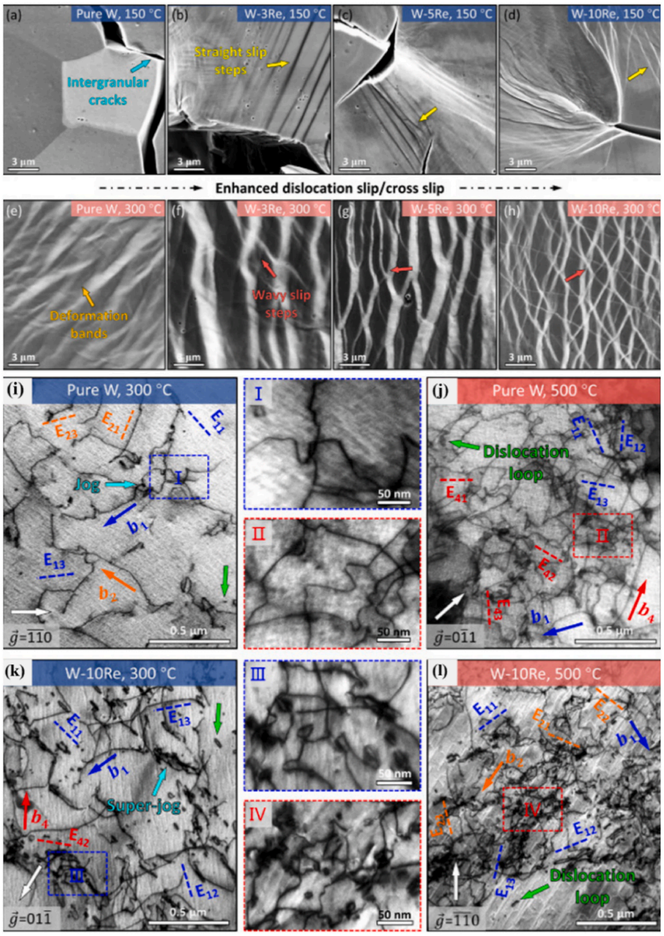

Fig. 9. (Reprinted from Ref. [168]) (a–h) SEM images of W/W-Re alloys after punching at 150 °C and 300 °C; The evolution of defect structures in W/W-Re alloys punched at 300 °C and 500 °C is presented, and bright-field TEM images show the dislocation structures of pure W (i–j) and W-10Re alloy (k–l) after punching.

content for the intended service temperature.

Ta is intrinsically ductile and may lower the activation barrier for dislocation motion. It also alters screw dislocation behavior, promotes long, straight screw dislocations and numerous loops, and provides solid-solution strengthening [169]. Ta-Re co-alloying has been explored to balance strength and toughness in W/Mo alloys, with reported grain sizes ranging from several micrometers to the nanoscale [170]. Ta also shows potential as an independent ductility-enhancing addition in W/Mo alloys. First-principles calculations by Zhang et al. [171] showed that Ta reduced the elastic constants of Mo alloys, produced a positive Cauchy pressure, and increased the B/G and Poisson ratios, indicating greater intrinsic ductility. Hu et al. [86] developed a high-accuracy machine learning potential (MLP) for W-Ta alloys. Large-scale molecular dynamics (MD) simulations likewise showed that Ta reduced the yield strength, elastic modulus, and stacking fault energy while increasing the bulk-to-shear modulus (B/G) and Poisson ratios. Ta also promoted dislocation nucleation and multiplication by weakening W-Ta bonding, thereby facilitating dislocation slip and plastic deformation. Ta may reduce reliance on Re in selected compositions but cannot be regarded as a direct substitute.

4.2. Line defect engineering

Dislocations are the principal line defects in crystalline materials [172,173]. BCC lattices lack close-packed slip planes and therefore exhibit high resistance to dislocation motion, particularly that of screw dislocations [84]. At low temperatures or high strain rates, dislocation mobility becomes limited, suppressing the onset of plastic flow. Accordingly, key design variables include dislocation density, mobility, character, and spatial arrangement, all of which depend on temperature, strain rate, and interstitial content. Kernel average misorientation (KAM) is a spatial proxy for local lattice curvature and can indicate trends in GND density [132], but it does not directly measure total dislocation density. The dislocation contribution to yield strength is commonly estimated using the Taylor equation [137]. The corresponding equations and parameters are provided in Supplementary Equations S8–S10.

High-density dislocations strengthen materials through entanglement, junction formation, and pile-ups. A moderate mobile dislocation density supports plastic flow, whereas excessive stored dislocations may concentrate stress and promote cracking. Thus, balancing mobile and stored dislocations is critical. Rolling and rotary swaging commonly introduce dislocations, but conventional multipass processing may accumulate strain slowly when per-pass deformation is limited, constraining strength-ductility synergy. Chen et al. [174] fabricated a Mo alloy containing irregular La_2O_3 nanoparticles. An ultrathin amorphous layer with a ridge-valley morphology formed between La_2O_3 and the Mo matrix (Fig. 10(c and d)). This interface absorbed vacancies and partially captured impinging dislocations, dividing them into segments and generating single-arm and Frank-Read sources (Fig. 10(a,b,f,g)). Dislocation multiplication persisted at −50 °C, and the alloy retained an elongation of 37%. Wang et al. [143] introduced a high dislocation density into a WHA through HPT. The large HPT-induced shear strain promoted dislocation multiplication, with dislocation density increasing with the number of revolutions. Dislocation strengthening was estimated to contribute more than 40% of the total strength. Controlled annealing can annihilate or rearrange residual dislocations, reducing lattice distortion and grain-boundary stress while retaining beneficial dislocation structures. Cheng et al. [175] found that the dislocation density in rotary-swaged W-0.5ZrC decreased from 1.2×10^{14} to 2.1×10^{13} m^{-2} after annealing at 1300 °C for 2 h through static recovery, annihilation, and rearrangement. This treatment reduced the obstruction of mobile dislocations by tangles while retaining grain refinement strengthening, yielding a strength of 710 MPa and a total elongation of 25%. Similarly, Liu et al. [176] regulated the dislocation density of a 91W-Ni-Fe-Co alloy by annealing at 500 °C for 3 h, reducing lattice distortion and grain boundary stress concentration. Enhanced dislocation mobility in the γ matrix promoted ductile tearing and fracture energy absorption, increasing the impact toughness to 175 J/cm^2.

Dislocations move by glide, climb, or cross-slip, whereas pinning impedes these processes [177]. The low mobility of $1/2\langle 111\rangle$ screw dislocations motivates alloying strategies that regulate their glide and cross-slip behavior. Feng et al. [169] found that Re improved ductility, whereas Ta reduced screw dislocation mobility, increased cross-slip frequency, and promoted long, straight screw segments. The higher loop density further pinned mobile dislocations and strengthened the alloy. Li et al. [178] reported that Nb promoted screw dislocation cross-slip in Mo single crystals, facilitating stable dislocation substructures and more uniform plastic flow. Moderate pinning can increase strength while preserving sufficient mobile dislocations for plastic deformation; excessive pinning may instead promote brittle fracture. Yuan et al. [35] constructed cellular substructures in a $W\text{-}Ni_{2.5}Fe\text{-}Co_{0.5}V_{0.6}$ alloy by DED. Nanoscale V-rich particles and vanadium oxides at cell boundaries impeded dislocation glide; some dislocations bypassed the particles and formed sessile structures reported as Lomer-Cottrell locks. Calculations using the Taylor hardening law estimated a dislocation strengthening contribution of approximately 203 MPa. Yang et al. [137] prepared Mo alloys with different B contents and found that dissolved B produced a solute drag effect. B atoms also formed Cottrell atmospheres that pinned dislocations, increasing dislocation accumulation and density with B content. During annealing, B

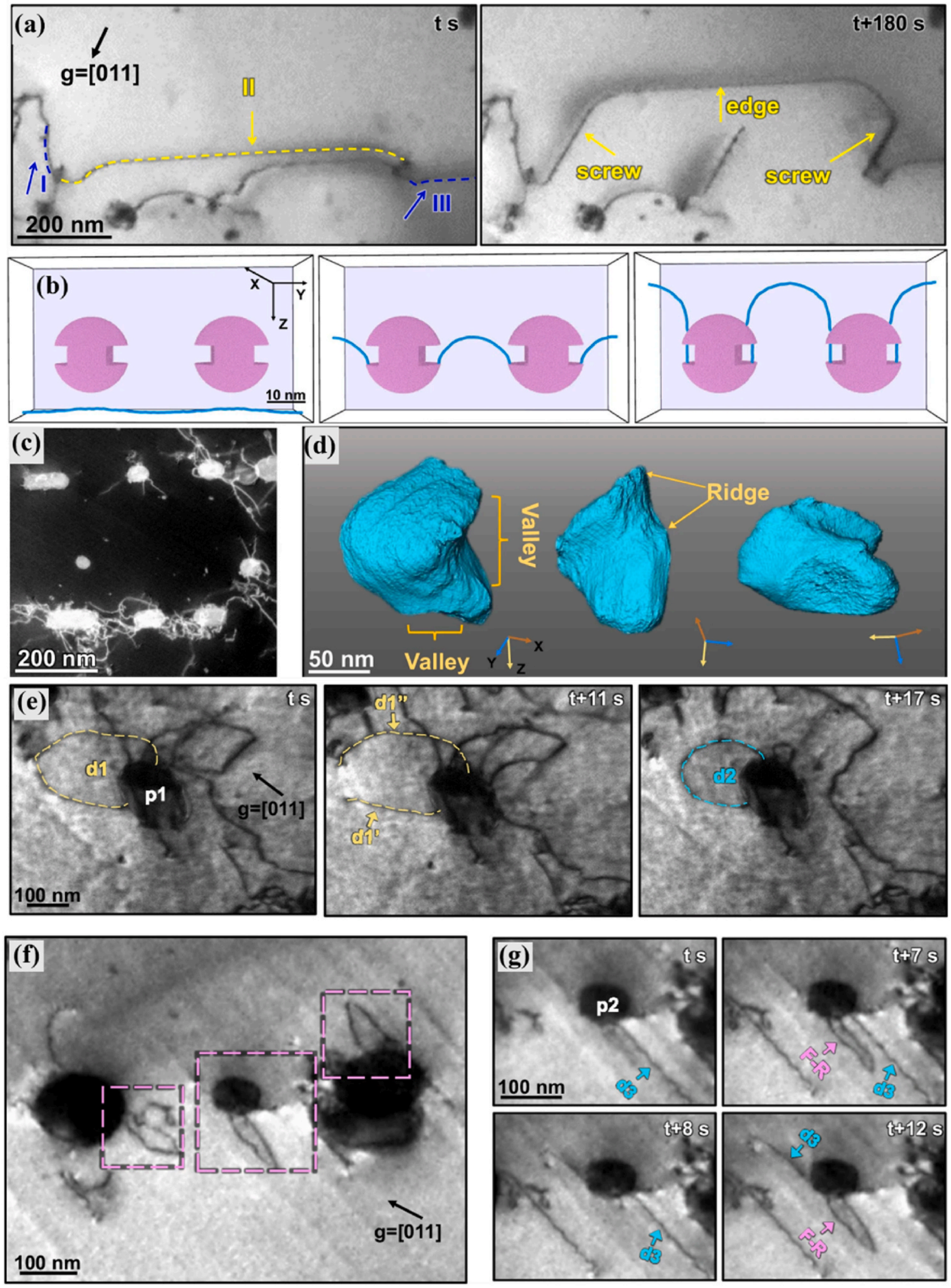

Fig. 10. (Reprinted from Ref. [174]) (a) In situ TEM tensile tests of sintered Mo-La_2O_3 alloy were conducted at room temperature, and second-phase particles divide dislocations into three segments; (b) MD simulation results; (c) Irregular morphology of La_2O_3 particles after rotary swaging and (d) corresponding 3D tomographic images; (e) Formation process of Frank-Read dislocation sources at room temperature; (f) Typical morphology of Frank-Read dislocation sources at −50 °C; (g) TEM images showing the dislocation multiplication induced by Frank-Read (F-R) dislocation sources during the interaction between dislocation segments and particle 2 under low temperature conditions.

further inhibited recovery, enabling the alloy to retain a tensile strength of 532.5 MPa and an elongation of 67.4% after treatment at 1200 °C.

Dislocation configuration describes the spatial arrangement of dislocations within a crystal. Disordered configurations, such as tangles, can concentrate stress. Ordered cells, subgrain boundaries, and dislocation walls impede slip and may improve strain accommodation and creep resistance through coordinated dislocation motion. In Mo single crystals, Li et al. [178] observed an Nb-dependent evolution of dislocation configurations. With increasing Nb content, dislocation walls in pure Mo evolved into dense, tangle-dominated cells in Mo-3Nb and then uniform cells in Mo-6Nb. These uniform cells may improve strain accommodation and creep resistance while retaining dislocation strengthening. This evolution was attributed to Nb-enhanced cross-slip of screw dislocations. Qian et al. [27] fabricated Mo-Re alloys with relative densities above 99% by L-PBF. The alloys contained dense dislocation walls, cellular structures, and low-angle subgrain boundaries that impeded dislocation slip and contributed to strengthening. Meanwhile, dislocations pinned by oxide particles acted as Frank-Read sources, sustaining dislocation multiplication and potentially balancing strengthening with plastic deformation.

4.3. Planar defect optimization

Planar defects, including grain and phase boundaries, impede dislocation motion but may also initiate or guide cracks when their cohesion is insufficient. Controlling their structure, chemistry, and distribution is therefore essential for tailoring the mechanical properties of W/Mo alloys and composites.

4.3.1. Grain refinement strengthening

Grain refinement is a well-established strengthening mechanism and may also contribute to toughening [96,179]. Finer grains increase grain boundary density and impede dislocation transmission. They may also redistribute strain and increase crack path tortuosity, although toughening requires cohesive and thermally stable grain boundaries. Within the conventional grain size regime, yield strength follows the Hall–Petch relation [129], with the grain boundary contribution expressed as σ_{gb} [137]. The corresponding equations and parameters are provided in Supplementary Equations S11–S13. Alloying and second-phase additions, combined with suitable processing, can refine grains with limited ductility loss and, in some cases, improved ductility.

Selected alloying additions can alter sintering or solidification, suppress grain coarsening, and refine grains. Chen et al. [180] found that Mo addition reduced W solubility in the γ-(Ni,Fe) matrix of W-Mo-Ni-Fe alloys. Mo enrichment in the liquid phase also slowed W particle coarsening, producing finer W grains. Shi et al. [181] showed that Nb lowered the WHA liquidus temperature and enabled lower-temperature LPS, accelerating particle rearrangement and densification while limiting W coarsening. The resulting 90W-0.5 wt% Nb alloy exhibited fine grains, an ultimate tensile strength of 924 MPa, and an elongation of 35%. Second-phase particles can also refine grains by pinning grain boundaries. Ji et al. [161] prepared TiC-doped Mo-based composites containing in situ formed Ti_3O_5 nanoparticles within grains and along grain boundaries, which suppressed grain growth. After SPS at 1200 °C, the average grain size was 1.3 μm (Fig. 11). The MT2 sample exhibited uniform grains and increased grain boundary density. Its KAM value of 0.21° and estimated GND density of 2.685×10^{14} m^{-2} exceeded those of pure Mo, indicating greater local lattice curvature. This trend is consistent with, but does not prove, grain-refinement-induced dislocation accumulation. The composite exhibited a compressive yield strength of 1340 MPa and a fracture strain above 50%. Liu et al. [28] refined TZM alloys through particle-stimulated nucleation (PSN). Micrometer-scale Zr-rich particles generated deformation zones that promoted recrystallization nucleation, refining the grains to approximately 1.5 μm. Meanwhile, semi-coherent nanoscale TiC precipitates pinned dislocations. The alloy exhibited a tensile strength of 939 MPa and an elongation of 27.4%.

Grain refinement generally strengthens W/Mo materials, whereas its toughening effect depends on grain boundary chemistry and thermal stability. Greater grain boundary area can redistribute strain but also increases susceptibility to impurity segregation, intergranular fracture, and high-temperature creep. Grain refinement often accompanies particle pinning and matrix purification. Its independent contribution must therefore be separated from these concurrent effects.

4.3.2. Grain boundary purification

Grain boundary purification reduces detrimental impurities or phases at grain boundaries, thereby improving intergranular cohesion [135]. In W/Mo alloys and composites, purification is commonly achieved by adding reactive elements or second-phase particles. These additions react with or trap impurities, reducing grain boundary segregation and suppressing the formation of brittle oxide films [31, 182]. This may improve both strength and ductility, provided that the reaction products do not themselves embrittle the grain boundaries.

Rare-earth elements have a strong affinity for detrimental impurities such as O and N in W/Mo materials. They react with grain boundary impurities, forming stable rare-earth oxides that suppress brittle phases and impede dislocation motion. However, these oxides may exhibit substantial lattice mismatch with the W/Mo matrix, resulting in weak interfacial bonding. Consequently, current efforts emphasize both uniform dispersion and interface control. Carbides such as TiC, ZrC, and TaC are promising for oxygen-related grain boundary purification because of their high melting points, thermal stability, and oxygen-scavenging ability [85,160]. Under suitable orientation relationships,

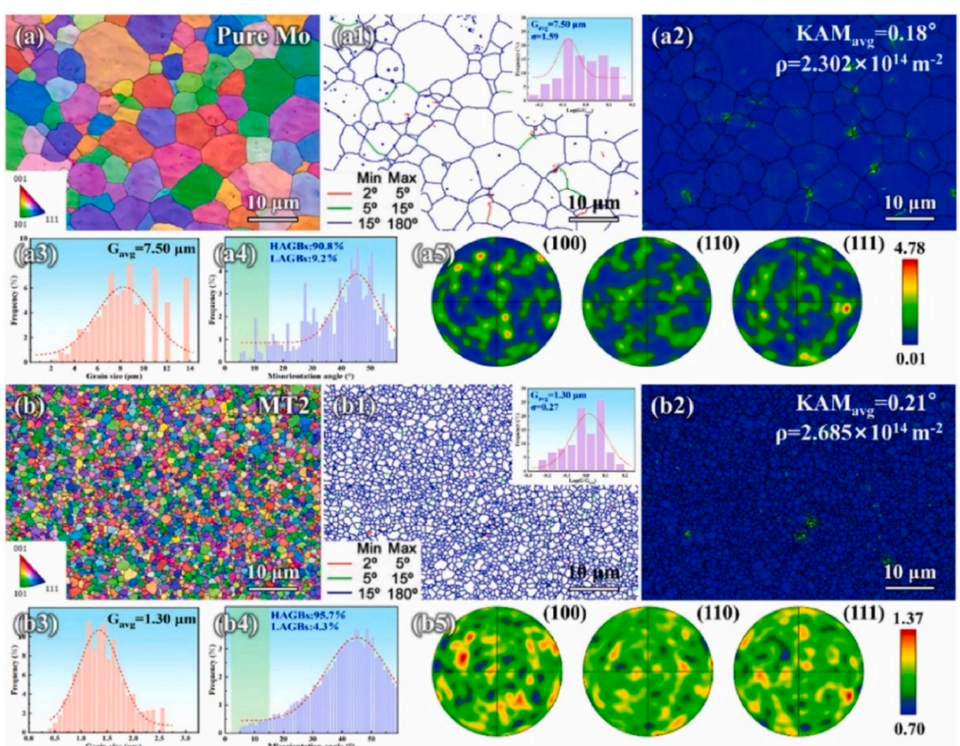

Fig. 11. (Reprinted from Ref. [161]) electron backscatter diffraction (EBSD) characterization maps of pure molybdenum (a) and MT2 sample (b), including inverse pole figure (IPF), grain boundary distribution map, KAM map, grain size distribution map, grain boundary misorientation distribution map and pole figure (PF).

these carbides may also form coherent or semi-coherent interfaces with W and Mo matrices. Hu et al. [155] added a small amount of TiC to a Mo alloy. During sintering, Ti_8C_5 adsorbed O impurities and formed TiO_x in situ, purifying the Mo matrix and grain boundaries. The resulting TiC/TiO_x particles formed coherent interfaces with Mo and contributed to matrix strengthening. The alloy achieved a high compressive strength of 1287.3 MPa and good ductility of 18.1%. Liu et al. [183] added TaC and Re to a W alloy and found that TaC captured O and was partially oxidized to Ta_2O_5. The composite containing 2.5 wt% TaC and 25 wt% Re exhibited a yield strength of 1.23 GPa and a strain capacity of 42%, supported by Re solid-solution strengthening. However, in oxygen-rich environments or when O content is poorly controlled, carbides may form brittle oxides or undergo decarburization, producing low-hardness phases.

Reactive elements can also scavenge impurities from grain boundaries. Yin et al. [141] prepared W-Hf alloys by PM followed by hot rolling. Hf reacted with O segregated at grain boundaries, forming dispersed HfO_2 particles. The HfO_2 particles scavenged O and refined the grains by boundary pinning. W-0.3 wt% Hf exhibited an ultimate tensile strength of 1048 ± 17 MPa at 100 °C, an elongation of 43.8 ± 1.5% at 500 °C, and a recrystallization temperature 200 °C above that of pure W. Chen et al. [184] added AlN particles to W-based composites produced by Fe-activated sintering. Fe segregated from the W(Fe) matrix to the AlN/matrix interface, where it reacted with AlN and O to form an approximately 2-nm-thick $(Fe,Al)_2O_3$ layer. This oxide layer scavenged O and stabilized the AlN particles. Combined with grain refinement and residual stress strengthening, these interfacial effects increased the microhardness, flexural strength, and fracture toughness by 101.4%, 66.3%, and 64.6%, respectively, relative to W(Fe).

4.3.3. Phase interface strengthening

Building on the bonding mechanisms discussed in Section 3.2, this subsection examines interfaces as mechanically active planar defects. Their contribution depends on coherency, effective load transfer without preferential interfacial cracking, and structural stability during processing and service. Coherent interfaces generally favor load transfer and particle stability, whereas semi-coherent or locally amorphous interfaces may better accommodate strain. The preferred interface state therefore depends on the material system and loading conditions; coherency alone does not define a universal hierarchy [30,152,157].

Interface orientation control and interfacial amorphization have emerged as strategies for improving interfacial compatibility and mechanical response. Dai et al. [185] found that Mn induced a Kurdjumov-Sachs orientation relationship between W and the γ phase in W-NiFeCoMn alloys, improving interfacial compatibility. During low-temperature tensile testing, Mn also promoted the formation of an 8.7-nm-thick amorphous layer at the W/γ interface. This buffer layer helped accommodate lattice mismatch and reduce interfacial stress concentration. Relative to W-NiFeCo, the elongation increased by 174.3% at room temperature and by 72.9% at −43 °C. Zhang et al. [186] prepared Mo-HfC alloys by PM followed by hot rolling, producing abundant LAGBs and a high fraction of grains with ⟨110⟩ parallel to the rolling direction (RD). These features promoted ordered dislocation networks and reduced susceptibility to intergranular brittle fracture. LAGBs also facilitated plastic deformation by offering less resistance to dislocation transmission than HAGBs. The Mo-0.5HfC alloy exhibited a room-temperature ultimate tensile strength of 950 MPa and a total elongation of 42.0%. Zhao et al. [187] prepared a W-0.2 wt% Al_2O_3 alloy by a wet-chemical method. Al_2O_3 particles reduced the average W grain size from 1 to 0.73 μm and increased the LAGB fraction. The increased LAGB fraction facilitated dislocation transfer and reduced pile-ups and strain mismatch, contributing to toughening. The alloy exhibited bending strengths of 1379 MPa at room temperature and 5090 MPa at 300 °C, together with a DBTT 100 °C below that of pure W.

4.4. Volume defect optimization

Although solid solution and dislocation strengthening increase strength, excessive strengthening can reduce ductility and toughness. Engineering beneficial three-dimensional features, particularly second phases, may mitigate this trade-off by controlling their size, distribution, and interfaces. When stable under service conditions, these features may balance strength and toughness while improving the high-temperature and irradiation resistance of W/Mo materials.

4.4.1. Second-phase strengthening

Second-phase engineering in W- and Mo-based materials includes particle dispersion strengthening [25,187], controlled precipitation, and fiber-mediated toughening in tungsten fiber-reinforced tungsten-matrix (W_f/W) composites.

Dispersion strengthening introduces stable oxide or carbide particles into a matrix [188]. Oxides are widely used in W/Mo materials and can be grouped into rare-earth oxides, such as Y_2O_3 and La_2O_3, and other oxides, such as Al_2O_3 and ZrO_2. Rare-earth oxides generally offer high thermal stability and coarsening resistance but are relatively costly. Other oxides are often cheaper and harder but may coarsen at high temperatures. In recent years, liquid-liquid doping and in situ precipitation have improved the dispersion of nanoscale oxide particles. Cui et al. [10] combined liquid–liquid doping with hydrothermal synthesis to mix Zr-containing precursors with Mo at the molecular level, yielding dispersed ZrO_2 nanoparticles. The ZrO_2 particles improved the mechanical response through Orowan strengthening, grain boundary pinning, and crack blunting. Yao et al. [189] prepared Mo-Y_2O_3 alloys by hydrothermal synthesis and SPS. The approximately 99-nm Y_2O_3 particles were uniformly dispersed and reportedly formed semi-coherent interfaces with Mo despite a lattice mismatch of approximately 15%, supporting load transfer. Their Orowan contribution to yield strength was estimated at 230–355 MPa. Compared with Y_2O_3, La_2O_3 is less chemically stable because of its greater hygroscopicity but is also less costly. Shakunt et al. [126] fabricated La_2O_3-reinforced W-Ni-Cu alloys. Dispersed La_2O_3 particles suppressed W particle coarsening through Zener pinning and increased W-W contiguity, thereby altering interparticle load transfer. However, contents above 1.0 wt% increased porosity and agglomeration, reducing densification and mechanical properties and highlighting the need for content control. Carbides are also promising reinforcements for improving the room-temperature mechanical properties of W alloys. Direct mixing with W powders can hinder sintering and produce nonuniform carbide distributions; in situ reactions [85] and dissolution-reprecipitation [190] can mitigate these problems. The grain boundary purification role of carbides is discussed separately in Section 4.3.2.

In recent years, high-entropy alloy design, as an extension of multicomponent solid-solution strengthening, has shown considerable potential for mitigating the intrinsic brittleness of refractory metals. Li et al. [191] proposed a strengthening and toughening strategy based on stepwise controllable coherent nanoprecipitations (SCCPs). Through stepwise thermomechanical processing, coherent δ nanolamellae and γ'' nanoparticles were sequentially formed within the FCC constituent of a dual-phase BCC/FCC W-based refractory high-entropy alloy. The coherent precipitate/matrix interfaces facilitated dislocation transmission and accommodation while alleviating local stress concentrations, enabling the alloy to achieve an ultimate tensile strength of 2.15 GPa and a uniform elongation of approximately 15% at room temperature. Similar design concepts have also been validated in other refractory high-entropy systems, where controlled precipitation has been shown to enhance strain-hardening capability and tensile ductility [192]. These studies demonstrate that integrating multi-principal-element compositional design with nanoscale precipitation control and interfacial optimization provides an important technological pathway for mitigating brittleness and improving the service reliability of refractory metals, including W and Mo.

Fiber toughening introduces continuous W fibers into a W matrix. Extrinsic mechanisms, including fiber bridging, pull-out, plastic deformation, and crack deflection, dissipate fracture energy and can improve fracture toughness [23,193]. Interfacial bonding and fiber microstructural stability are therefore central to W_f/W composite design. Under the tested conditions, Gietl et al. [194] ranked the energy contributions as fiber plastic deformation > fiber bridging > interfacial debonding > crack deflection. Y_2O_3-based interface modification has been widely explored in W_f/W composites. Chen et al. [195] showed that Y_2O_3 coatings formed weakly bonded interfaces, suppressed abnormal surface grain growth during low-temperature sintering, and limited fiber embrittlement. Shu et al. [193] prepared continuous fiber-reinforced W_f/Y_2O_3/W composites by PM and linked their toughening behavior to the interfacial debonding length. Sufficient debonding permits fiber plastic deformation, whereas insufficient debonding promotes premature brittle fracture. To avoid nonuniform coating thickness, damage, and peeling, Chen et al. [23] directly added Y_2O_3 particles to the matrix. During sintering, Y_2O_3 particles migrated to fiber–matrix interfaces and reduced interfacial bonding strength. Matrix addition is simpler and less costly than coating but provides less uniform fiber protection and interface control. Chen et al. [196] introduced Re into W_f/W composites, increasing their relative density (Fig. 12(a–f)). However, Re also accelerated abnormal recrystallization of the W fibers. At 1100 °C, weak interfaces promoted debonding and fiber pull-out. As the sintering temperature increased, cleavage fracture became more prevalent. Above 1400 °C, stronger fiber–matrix bonding and recrystallization-induced embrittlement produced mixed intergranular and cleavage fracture (Fig. 12(g–n)). These results show that Re-induced densification must be balanced against interface strengthening and fiber recrystallization.

4.4.2. Void and microcrack tailoring

Pores concentrate stress, whereas unstable microcrack propagation can trigger brittle fracture. Recent work, particularly on W-based materials, has expanded from defect elimination to controlled pore utilization and in situ microcrack repair.

In W_f/W composites, a dense matrix provides strength, whereas excessive interfacial bonding suppresses fiber pull-out. Mao et al. [197] introduced controlled matrix porosity to redirect cracks toward fiber–matrix interfaces and increase crack path tortuosity. The W fibers then dissipated fracture energy through bridging and pull-out. However, a fiber fraction of 60% degraded performance because the powder could not fully fill the inter-fiber spaces, leaving residual pores. Hu et al. [198] investigated the effect of post-sintering temperature on AM-fabricated 93W-4.6Ni-2.4Fe. At 1480 °C, the liquid γ phase filled interparticle pores through capillary-driven flow, increasing the relative density above 99.5%. A continuous γ phase network also formed at 1480 °C. Dense, uniformly distributed dimples indicated plastic energy absorption, while the γ phase bridged microcracks. The alloy exhibited a tensile strength of 1040 ± 6 MPa and an elongation of 20.7 ± 0.4%. Microcrack initiation and propagation also govern brittle fracture in W-based materials. Alam et al. [199] found that annealing hot-rolled 90W7Ni3Fe at 1300 °C for 24 h increased its fracture toughness to 125 ± 12 MPa $m^{1/2}$ and elongation to 15%. This improvement was attributed to microcrack shielding. In the annealed alloy, dispersed microcracks formed near the main crack tip during loading, creating a dilatational shielding zone. These microcracks redistributed stress, reduced the stress intensity factor at the main crack tip, and consumed energy during formation and propagation. Unlike microcrack shielding, Gao et al. [26] reported a liquid-phase crack-filling mechanism. Because ZrO_2 melts at 2715 °C, below W at 3422 °C, it can flow into thermally induced cracks and pores while the W matrix remains solid. Small cracks could be filled, whereas larger cracks became discontinuous, reducing crack connectivity and propagation. The resulting W ZrO_2 composite exhibited a relative density of 98.82% and a compressive strength of 1694 MPa.

4.4.3. Phase transformation strengthening

Phase transformation strengthening and toughening exploit transformation-induced strain, energy dissipation, and pinning by transformation products to reduce crack-tip stresses and impede dislocation and crack motion, potentially improving the strength-toughness balance.

Conventional W and Mo lack a transformation-induced plasticity (TRIP) mechanism analogous to the austenite-to-martensite transformation in steels. The stress-induced martensitic transformation of ZrO_2 from its tetragonal to monoclinic phase (t-ZrO_2 → m-ZrO_2) produces volume expansion and is widely used to toughen ceramics. However, introducing this mechanism into W or Mo matrices presents two challenges. The matrix must constrain metastable t-ZrO_2 against spontaneous transformation at room temperature, while crack-tip stresses must trigger transformation before brittle fracture occurs. Mao et al. [165] added Zr to a W-Ni_3Al alloy, where it reacted with O during sintering to form metastable t-ZrO_2. This phase was retained at room

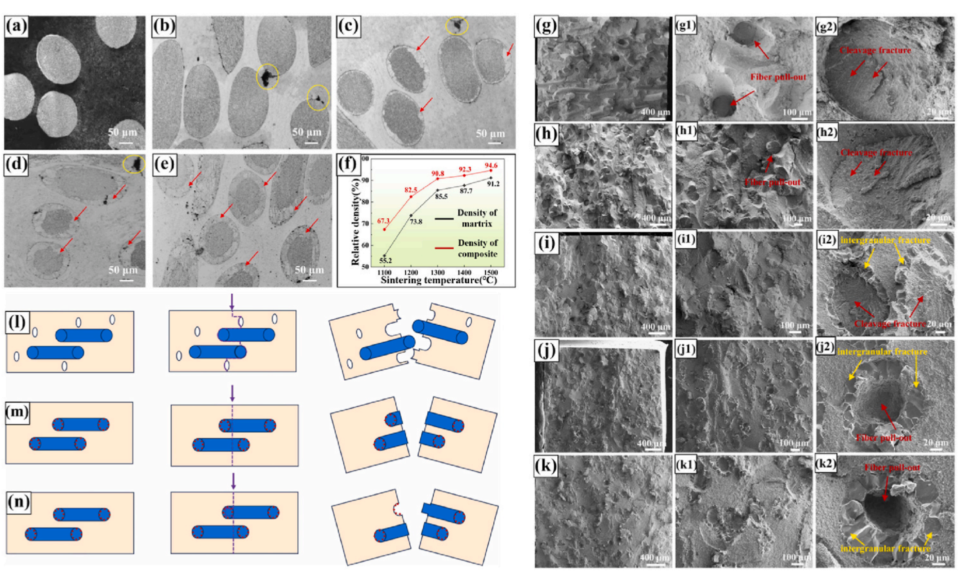

Fig. 12. (Reprinted from Ref. [196]) Optical micrographs of W_f/W-Re composites sintered at (a) 1100 °C, (b) 1200 °C, (c) 1300 °C, (d) 1400 °C, and (e) 1500 °C; (f) relationship between relative density and sintering temperature for the W-Re matrix and composites. Fracture surfaces of W_f/W-Re composites sintered at (g) 1100 °C, (h) 1200 °C, (i) 1300 °C, (j) 1400 °C, and (k) 1500 °C. Schematic fracture modes at (l) low, (m) intermediate, and (n) high sintering temperatures.

temperature by rapid SPS cooling and the stabilizing effect of Al_2O_3. Under loading, crack-tip stress concentration triggered the t-ZrO_2 → m-ZrO_2 transformation. The transformation-induced expansion generated compressive stresses that reduced local tension and promoted crack deflection and closure. The alloy exhibited a bending strength of approximately 1473 MPa. Du et al. [200] prepared ceria-partially stabilized zirconia (Ce-PSZ)-reinforced Mo alloys by hydrogen sintering at 1900 °C. Ce^{4+} stabilized t-ZrO_2 in the Mo matrix against spontaneous transformation. During loading, dislocations accumulated at phase boundaries and generated local stresses that triggered the t-ZrO_2 → m-ZrO_2 transformation. At 1.5 wt% Ce-PSZ, the alloy exhibited the reported optimal property combination: an ultimate tensile strength of 528.5 MPa, an elongation of 29.3%, and a fracture toughness of 38.5 MPa $m^{1/2}$. Beyond zirconia toughening, precipitation and matrix phase transformations provide additional strengthening and toughening routes. Lin et al. [201] aged as-forged Mo-47.5Re at 1600 °C and observed Re diffusion and enrichment along grain boundaries. Once the local Re content reached a critical level, coherent $MoRe_2$ σ phase precipitates formed and produced precipitation hardening. The alloy exhibited a yield strength of 600 MPa and a uniform strain of 21.5%. Mo normally adopts a stable BCC structure. First-principles calculations indicate that increased d-electron occupancy through Re alloying or applied strain may stabilize face-centered cubic (FCC) Mo. A metastable FCC phase may improve compressive ductility through transformation-induced plasticity. Yu et al. [202] reported a BCC-to-FCC transformation in a Mo matrix. Severe deformation during high-energy ball milling, followed by rapid SPS heating and cooling, retained 1.9 vol % metastable FCC Mo in a Mo-14Re-1Y_2O_3 alloy. Two martensitic orientation relationships were identified between the BCC matrix and FCC phase: Kurdjumov-Sachs (K-S) and Nishiyama-Wassermann (N-W). The metastable FCC phase, together with Zener pinning by Y_2O_3 particles, contributed to a yield strength of 1218 MPa and a compressive strain of 37.6%.

5. Irradiation resistance mechanism

The ultimate purpose of the strengthening and toughening strategies discussed above is to ensure the reliable performance of W/Mo materials under demanding service conditions. However, in nuclear and fusion environments, the effectiveness of these strategies cannot be evaluated solely on the basis of mechanical properties.

Owing to its ultrahigh melting point, low sputtering yield, high-temperature stability, and low hydrogen isotope retention, W is a leading candidate for plasma-facing components (PFCs) in the International Thermonuclear Experimental Reactor (ITER) [2,3]. Similarly, Mo and its alloys are candidates for core structures and cladding in space nuclear reactors because of their elevated-temperature strength, weldability, and compatibility with nuclear fuels [7,31]. However, both W- and Mo-based materials are susceptible to damage under intense irradiation. Irradiation damage begins when energetic particles, such as neutrons or ions, collide with lattice atoms and generate primary knock-on atoms (PKAs) [3]. PKAs initiate displacement cascades that generate Frenkel pairs comprising vacancies and self-interstitial atoms [14,203]. After cascade relaxation, surviving vacancies and self-interstitial atoms migrate, recombine, or aggregate. Small defect clusters commonly appear as black-dot defect clusters in TEM, whereas larger interstitial clusters can form dislocation loops and vacancy clusters can evolve into nanovoids. In He-containing irradiation environments, He-vacancy complexes nucleate nanobubbles; their growth and coalescence near the surface can cause blistering, whereas sustained low-energy, high-flux He exposure at elevated temperatures may generate a porous fuzz layer. The accumulation of these defects contributes to irradiation hardening and embrittlement, swelling, surface degradation, and DBTT elevation [204]. Fig. 13 presents representative irradiation-induced defects and morphologies. Mitigating these defects and improving the irradiation resistance of W/Mo materials are

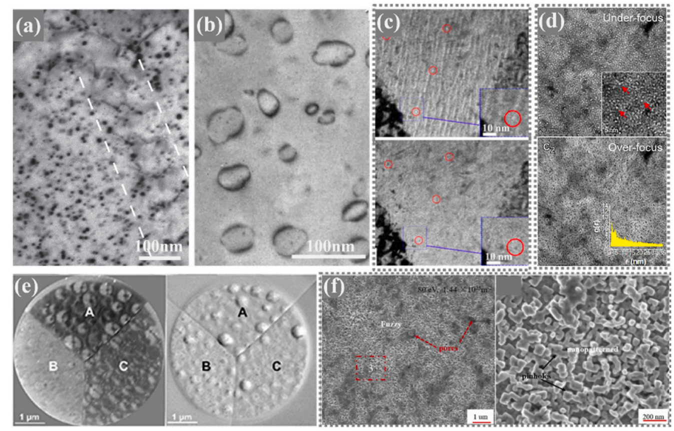

Fig. 13. Representative irradiation-induced defects and surface damage in W- and Mo-based materials. (a) Black-dot defect clusters and a defect-depleted zone associated with a dislocation array in Mo-14Re observed by bright-field TEM (reprinted from Ref. [205]); (b) dislocation loops in Mo-5Re observed by bright-field TEM (reprinted from Ref. [32]); (c) vacancy-type voids in W-3Re revealed by under- and over-focused TEM (reprinted from Ref. [206]); (d) He bubbles in pure W revealed by under- and over-focused TEM (reprinted from Ref. [207]); (e) He-induced surface blistering in pure W observed by in situ helium ion microscopy (left) and SEM (right) (reprinted from Ref. [208]); and (f) He-plasma-induced fuzz and its corresponding nanopatterned surface morphology in pure W observed by SEM (reprinted from Ref. [150]).

therefore of considerable importance. Existing studies have employed distinct irradiation modes. Low-energy, high-flux He plasma exposure is mainly used to investigate near-surface gas retention and surface morphology, whereas He-ion and He/H dual-beam irradiation introduce implanted gases together with displacement damage over finite projected ranges. High-energy Kr-ion irradiation enables the accelerated generation of shallow displacement damage, with a distinct cascade spectrum and implanted-ion profile, whereas neutron irradiation produces bulk damage and neutron-spectrum-dependent transmutation effects. Consequently, bubble sizes and damage levels reported under these different irradiation conditions are not directly compared in this review. In this section, irradiation-resistance strategies for W/Mo materials are broadly categorized into three groups: defect trap engineering, conventional alloying-element modulation, and high-entropy alloy design.

5.1. Defect trap engineering

Defect trap engineering introduces a high density of microstructural features that can act as defect traps or sinks, including grain boundaries, phase boundaries, dislocations, and precipitates. These features can trap He/H atoms and defect clusters, whereas extended sinks absorb mobile vacancies and SIAs and promote vacancy-interstitial recombination.

As two-dimensional defects, grain and phase boundaries can act as sinks for mobile vacancies and SIAs and as traps for He atoms because of their excess free volume and high interfacial energy. Li et al. [160] prepared nanostructured TiC dispersion-strengthened W-based composites containing semi-coherent W/TiC interfaces with approximately 25-nm-thick interdiffusion layers. First-principles calculations showed that the He migration barrier was 1.15 eV at the W/TiC interface, compared with 0.43 eV in W. Among the sites considered, the phase boundary was the most stable He trap, with a trapping energy of 4.07 eV. After irradiation, the W-TiC composite exhibited a damage depth of 9.53 μm, approximately half that of pure W, and smaller He bubbles with an average size of 16 nm. Similarly, Lv et al. [150] prepared a fine-grained W-0.3 wt% Y_2O_3 composite containing semi-coherent Y_2O_3/W interfaces. Grain and phase boundaries acted as transient He traps and preferential transport pathways, capturing He from the lattice and facilitating its migration to the surface. After He plasma irradiation at 60–80 eV to a fluence of 2.3×10^{26} m^{-2}, no discernible nanofuzz or He bubbles were observed in the composite. The fluence required to produce surface damage comparable to that of pure W was two to three orders of magnitude higher.

As one-dimensional defects, dislocations interact elastically with point defects, promoting their segregation and recombination near dislocation cores. Dislocation morphology therefore strongly influences irradiation defect evolution. Huang et al. [209] investigated the effects of pre-existing dislocation on bubble evolution in W-0.5ZrC under dual-beam He^{+} and H_2^{+} irradiation at 900 °C. Pre-existing dislocations acted as strong defect sinks, absorbing mobile point defects and reducing matrix bubble nucleation, thereby changing the bubble distribution from homogeneous to heterogeneous. Straight dislocations promoted bubble growth but suppressed nucleation; curved dislocations mainly suppressed nucleation; interlaced networks suppressed both processes. At 0.726 displacements per atom (dpa), swelling in high-dislocation-density regions was 54% of that in dislocation-free regions, supporting the bubble suppression effect. Li et al. [205] conducted in situ irradiation of a Mo-14Re model alloy using 800 keV Kr^{2+} ions. The observed microstructure contained three interwoven sets of 1/2⟨111⟩ dislocation arrays that constituted low-angle subgrain boundaries. Under irradiation, dislocation reactions produced stable binary ⟨100⟩ and ternary 1/2⟨111⟩ sessile junctions, forming a topologically locked network. Junction anchoring prevented long-range network motion, whereas segments between junctions bowed directionally under irradiation-induced displacement cascades. This network provided abundant sinks for irradiation-induced point defects while limiting large-scale dislocation rearrangement and microstructural instability.

5.2. Alloying element modulation

Alloying elements can interact with irradiation-induced defects and alter their migration and aggregation, thereby mitigating damage accumulation. A mixed dumbbell is an interstitial configuration in which a matrix atom and a solute atom form a paired structure around a lattice site. Mixed dumbbells can alter self-interstitial atom (SIA) migration, trap He, and suppress defect clustering and bubble growth. Wang et al. [210] found that stable W-Re mixed dumbbells underwent rapid, short-range three-dimensional motion, promoting vacancy–interstitial recombination. This behavior has motivated extensive research on Re alloying for irradiation resistance. However, at high doses and temperatures, Re can undergo irradiation-induced segregation and precipitation, causing hardening [211].

In W alloys, the effect of Re on irradiation resistance is strongly dose-dependent. Li et al. [212] used object kinetic Monte Carlo (OKMC) simulations to construct an irradiation response transition map for W-2Re. At low doses and temperatures above 773 K, Re formed stable Re-SIA complexes. These complexes recombined with thermally mobile vacancies, promoting vacancy-interstitial annihilation. At higher doses, however, this beneficial effect diminished as Re aggregated and precipitated into Re-rich phases. Molecular dynamics simulations by Yang et al. [213] further showed that Re segregated to dislocation loops and formed Re-loop complexes. Above a local Re concentration of 15 at. %, these complexes changed from weak to strong obstacles, pinning edge dislocation glide and promoting irradiation hardening. Neutron irradiation experiments by Gietl et al. [214] showed that pure W and W-3% Re underwent irradiation-enhanced recrystallization at 850 °C, whereas thermal annealing at the same temperature caused no grain growth. This behavior was attributed to irradiation-enhanced diffusion mediated by neutron-induced Frenkel defects. Under irradiation at 850 °C, the W self-diffusion coefficient approached that during thermal annealing at 1200 °C, becoming sufficient for recrystallization. Transmutation-generated Re and Os also formed highly mobile mixed dumbbells with W, further increasing self-diffusion. This enhanced diffusion counteracted Re-induced inhibition of grain boundary migration, promoting grain growth in W-3% Re. The study also showed that La-derived La_2O_3 particles remained stable during high-temperature irradiation and suppressed grain growth through boundary pinning. K doping also formed nanobubbles that pinned grain boundaries and limited W-SIA migration and vacancy accumulation [215]. However, K bubble pinning became ineffective under high-temperature irradiation. In Mo-Re alloys, irradiation can induce defect accumulation and Re-rich precipitation. First-principles and molecular statics calculations by Sun et al. [33] predicted that Re could reduce the intrinsic room-temperature brittleness of Mo. Under irradiation, Re strongly interacted with vacancies to form V-Re pairs, suppressing vacancy clustering. At higher vacancy concentrations, these pairs evolved into V_2-Re_1 complexes that nucleated Re-rich clusters. These clusters were predicted to become the dominant defect structures in Mo-Re alloys under high-temperature irradiation. Ti, Zr, and Nb have been explored as auxiliary solutes to complement Re in improving the irradiation resistance of Mo alloys. Cui et al. [32] found that all three solutes increased relevant defect formation energies and migration barriers in Mo-5Re. These effects suppressed loop climb and coalescence, maintaining fine, dispersed loops. Among the three solutes, Nb bound interstitial He most strongly, producing the smallest loops and He bubbles in Mo-5Re-0.5Nb. By contrast, Zr most effectively suppressed overall swelling under the simulated conditions.

5.3. High entropy alloy effect

Some conventional W-based binary alloys, such as W-Re and W-Ti, can undergo embrittlement and irradiation-induced precipitation. By contrast, HEAs are multicomponent systems containing several principal elements, often in near-equiatomic proportions. High configurational entropy may favor simple solid solution phases, while HEAs are often associated with lattice distortion, sluggish diffusion, and cocktail effects. These effects may hinder defect migration and phase separation, making selected HEAs promising irradiation-resistant materials.

The irradiation resistance of HEAs is commonly associated with three mechanisms [216,217]. First, chemical complexity and lattice distortion broaden defect formation and migration energy distributions, altering vacancy and interstitial transport and potentially promoting recombination. Second, reduced effective defect mobility may suppress dislocation loop and He bubble growth, although this effect depends on composition and temperature. Third, Cr- or V-rich precipitates and their interfaces can provide additional sinks for point defects [218]. Wang et al. [207] designed a $W_{15}Ta_{15}Cr_{35}V_{35}$ multicomponent alloy with high irradiation tolerance. After 3 h of 400-keV He^{+} irradiation at room temperature or 450 °C, the alloy showed less irradiation hardening and smaller matrix He bubbles than pure W. This behavior was attributed to two mechanisms. First, lattice distortion in the disordered solid solution restricted long-range vacancy and He migration, promoting localized motion and dispersed bubble nucleation. Second, interstitial C introduced during rapid hot-press sintering combined with alloying elements to form coherent, C-rich ordered nanoprecipitates. The associated C-containing complexes had higher migration barriers than isolated vacancies, enabling vacancy trapping and suppressing He nucleation and aggregation. Supakul et al. [219] prepared low-activation W-Ti-Cr-V refractory alloys by arc melting and DED. Under He and Kr ion irradiation at 900 °C to doses of at least 10 dpa, alloys produced by both routes showed limited damage accumulation. The complex chemical environment and energy landscape promoted point defect recombination and limited the formation of vacancy clusters and dislocation loops. The homogeneous arc-melted microstructure was associated with more uniform defect distributions and recombination. Although the DED samples showed region-dependent responses because of compositional heterogeneity, severe defect accumulation remained limited. These mechanisms vary with HEA composition and irradiation temperature. Most supporting data derive from a limited range of ion irradiation conditions. Before direct comparison with conventional W/Mo alloys, phase stability, thermal conductivity, activation behavior, and post-irradiation toughness require further validation.

6. Conclusions and prospects

This review establishes a preparation–microstructure–property framework for W- and Mo-based refractory alloys and composites intended for extreme service environments. Based on recent advances in this field, three main conclusions can be drawn. (1) Processing routes: PM, particularly SPS, remains advantageous for material densification and grain refinement. AM offers flexibility for the near-net-shape fabrication of complex components but still faces challenges related to cracking, porosity, and impurity control. Therefore, processing route selection should account for component geometry and service requirements. (2) Homogeneous microstructures favor the uniform dispersion of second phases and enhanced thermal stability, whereas heterogeneous microstructures can improve mechanical properties through strain partitioning and HDI strengthening. However, simultaneous improvements in strength and toughness should be evaluated using comparable data obtained under consistent testing and service conditions. (3) Mechanistic understanding: Thermodynamic driving forces and kinetic constraints jointly govern microstructural evolution. Coherent or semi-coherent interfaces can facilitate load transfer, whereas stable defect traps can capture irradiation-induced defects and suppress their migration and aggregation. Both effects depend on interface chemistry, trap capacity, temperature, irradiation dose, and microstructural stability. In addition, multidimensional defect engineering can integrate solid-solution strengthening, dislocation strengthening, grain refinement, grain boundary purification, second-phase strengthening, and phase transformation strengthening, providing a potential route toward an improved strength-toughness balance.

Current research nevertheless has several limitations. First, high-performance alloy compositions and microstructural architectures may rely on costly elements or complex processing routes, while reproducible component-scale control over density, defects, interfaces, and microstructural heterogeneity has not yet been sufficiently demonstrated. Second, although AM has become an increasingly prominent near-net-shape manufacturing technology in recent years, challenges associated with processing defects, dimensional accuracy, and large-scale production remain to be overcome. Finally, the evidence base for assessing long-term service reliability remains fragmented. Existing studies have largely focused on the mechanical properties and irradiation resistance of W- and Mo-based materials, and these topics therefore constitute the principal focus of the present review. However, the fundamental understanding of coupled oxidation-volatilization mechanisms in W and Mo under extreme service conditions remains insufficient, while the available studies on fatigue performance are also limited and heterogeneous.

Future research should prioritize the following directions: (1) developing in situ and multimodal characterization techniques under coupled multiphysics conditions to reveal defect evolution and crack initiation; (2) establishing standardized multi-property evaluation systems that jointly report strength, ductility, fracture toughness, thermophysical properties, oxidation resistance, and irradiation stability under clearly specified testing conditions; (3) constructing a closed loop linking multiscale simulation, material processing, and service behavior. First-principles calculations [220,221], molecular dynamics simulations [222–224], and Monte Carlo simulations [225] should be integrated with experiments to connect electronic- and atomic-scale mechanisms with microstructural evolution and service-scale radiation responses. Interpretable machine learning [226,227] can also assist in screening alloy compositions and processing parameters, provided that the underlying data are traceable and comparable. (4) Systematically investigating high-temperature oxidation, mechanical fatigue, thermomechanical fatigue, and their coupled effects under representative service conditions to enhance the long-term service reliability of W- and Mo-based materials. (5) concurrently developing cost-effective alloying strategies, robust and reliable PM and AM processes, and component-scale validation methods to facilitate the transition of high-performance W- and Mo-based materials from laboratory research to engineering applications.

Declaration of competing interest

The authors declare that they have no known competing financial interests or personal relationships that could have appeared to influence the work reported in this paper.

Acknowledgements

This work was supported by National Natural Science Foundation of China (No. 52503412), the Fundamental Research Funds for the Central Universities (No. 2682026CX129).

Appendix A. Supplementary data

Supplementary data to this article can be found online at https://doi.org/10.1016/j.jmrt.2026.09.068.

References

[1] Wu Y. Manufacturing of tungsten and tungsten composites for fusion application via different routes. Tungsten 2019;1:80–90. https://doi.org/10.1007/s42864-019-00011-y.
[2] Yang T, Wang H, Feng F, Liu X, Gong X-Y, Lian Y-Y, et al. Comparison of thermal shock resistance capabilities of the rotary swaged pure tungsten, potassium-doped tungsten, and W-La_2O_3 alloys. Tungsten 2024;6:759–66. https://doi.org/10.1007/s42864-024-00270-4.
[3] Kazakov A, Babicheva RI, Zinovev A, Terentyev D, Zhou K, Korznikova EA, et al. Interaction of edge dislocations with voids in tungsten. Tungsten 2024;6:633–46. https://doi.org/10.1007/s42864-023-00250-0.
[4] Jin Y-Z, Liu X, Lian Y-Y, Song J-P. Influence of recrystallization on tungsten divertor monoblock under high heat flux. Tungsten 2022;4:194–202. https://doi.org/10.1007/s42864-021-00126-1.
[5] Wang P-J, Cao Q, Liu S, Peng Q. Fragility under shocking: molecular dynamics insights into defect evolutions in tungsten lattice. Tungsten 2021;3:234–42. https://doi.org/10.1007/s42864-021-00087-5.
[6] Ge S-W, Hu P, Deng J, Li S-L, Xing H-R, Han J-Y, et al. The effect of secondary phase on corrosion behaviors of the titanium–zirconium–molybdenum alloy. Tungsten 2024;6:342–54. https://doi.org/10.1007/s42864-023-00228-y.
[7] Li F, Chen C, Guo D, Zhou X, Chen Y, Long Y, et al. Rate theory and experimental study of the irradiation induced defects in molybdenum alloy. J Alloys Compd 2021;874:159751. https://doi.org/10.1016/j.jallcom.2021.159751.
[8] Xu H, Huang L, Zhang W, Liang J, Lin X, Zhang X, et al. Mechanical and microstructural responses in molybdenum-rhenium alloys under hot compressions. J Mater Res Technol 2024;30:3877–85. https://doi.org/10.1016/j.jmrt.2024.04.063.
[9] Cui C, Wu M, Zhu X, Liu Q, Ma D, Wang H, et al. Mechanism of zirconia in suppressing cracking during thermal deformation of molybdenum alloys. J Alloys Compd 2025;1047:185104. https://doi.org/10.1016/j.jallcom.2025.185104.
[10] Cui C, Duan H, Zhu X, Wu M, Fan M, Liu Q, et al. Evaluation of tensile property and strengthening mechanism of zirconia reinforced molybdenum alloy. J Alloys Compd 2023;967:171716. https://doi.org/10.1016/j.jallcom.2023.171716.
[11] Huan J, Wu Z, Wang Q, Zhang S, Kwon S-H. A comparative investigation on the microstructure and thermal resistance of W-film sensor using dc magnetron sputtering and high-power pulsed magnetron sputtering. Magnetochemistry 2023;9:97. https://doi.org/10.3390/magnetochemistry9040097.
[12] Ding C-J, Lei Y-W, Wang X-Y, Li X-L, Li X-Y, Zhang Y-G, et al. A deep learning interatomic potential suitable for simulating radiation damage in bulk tungsten. Tungsten 2024;6:304–22. https://doi.org/10.1007/s42864-023-00230-4.
[13] Hu B, Quan C, Zhao X, Xing H, Shi Z, Yi S, et al. Microstructure and performance optimization of molybdenum alloys reinforced by zirconium carbide whiskers. J Alloys Compd 2026;1058:187078. https://doi.org/10.1016/j.jallcom.2026.187078.
[14] Wu Z-M, He L, Ye L-S, Yang X-F, Zhang J-J, Lei H-B. High-dense nanocrystalline W-based alloy prepared by hot isostatic pressing with uniform microstructure, ultrahigh hardness and good thermal stability. Tungsten 2024;7:120–36. https://doi.org/10.1007/s42864-024-00296-8.
[15] Pan S-H, Yao G-C, Cui Y-N, Meng F-S, Luo C, Zheng T-Q, et al. Additive manufacturing of tungsten, tungsten-based alloys, and tungsten matrix composites. Tungsten 2022;5:1–31. https://doi.org/10.1007/s42864-022-00153-6.

[16] Omole S, Lunt A, Kirk S, Shokrani A. Advanced processing and machining of tungsten and its alloys. J Manuf Mater Process 2022;6:15. https://doi.org/10.3390/jmmp6010015.
[17] Zarinejad M, Tong Y, Salehi M, Mu C, Wang N, Xu Y, et al. Advancements and perspectives in additive manufacturing of tungsten alloys and composites: challenges and solutions. Crystals 2024;14:665. https://doi.org/10.3390/cryst14070665.
[18] Li H, Shen Y, Wu X, Wang D, Yang Y. Advances in laser powder bed fusion of tungsten, tungsten alloys, and tungsten-based composites. Micromachines 2024;15:966. https://doi.org/10.3390/mi15080966.
[19] Leclercq A, Mouret T, Brailovski V. Laser powder bed fusion of molybdenum: density, structure and mechanical properties at room and elevated temperatures. Mater Sci Eng, A 2025;929:148004. https://doi.org/10.1016/j.msea.2025.148004.
[20] Liu J, Zavdoveev A, Klapatyuk A, Baudin T, Kozin R, Gajvoronskiy A, et al. Exploring the influence of melting techniques on high entropy alloys: WAAM versus plasma arc and vacuum melting. Mater Lett 2025;397:138846. https://doi.org/10.1016/j.matlet.2025.138846.
[21] Wang R, Zhu Z, Li N, Yan D, Cui B, Huang S, et al. Laser directed energy deposition of ceramic/metal composites: interfacial modification and heat input regulation for tailored microstructure and enhanced mechanical properties exemplified by high boron steel. Compos Part A Appl Sci Manuf 2026;205:109689. https://doi.org/10.1016/j.compositesa.2026.109689.
[22] Sun J, Yin M, Yang J, Gu D. Laser powder bed fusion of tungsten alloy containing a high content of low-melting-point metallic phase: densification behavior, microstructure evolution, and mechanical properties. Int J Refract Met Hard Mater 2025;131:107238. https://doi.org/10.1016/j.ijrmhm.2025.107238.
[23] Chen Y, Chen C, Chen JH, Li KL, Wang S, Zhang YF, et al. The effect of Y_2O_3 particles on the microstructure and mechanical properties of tungsten fiber-reinforced tungsten composites. Mater Sci Eng, A 2024;918:147449. https://doi.org/10.1016/j.msea.2024.147449.
[24] Wang G, Xiong N, Kuang C. Effect of La_2O_3 on the properties of molybdenum rhenium alloy. Int J Refract Met Hard Mater 2024;122:106717. https://doi.org/10.1016/j.ijrmhm.2024.106717.
[25] Hu B, Quan C, Ma S, Zhang Q, Xing H, Wang L, et al. Strengthening-toughening mechanism of carbon-coated TiC/ZrC secondary phase doped molybdenum alloy. Mater Sci Eng, A 2025;929:148096. https://doi.org/10.1016/j.msea.2025.148096.
[26] Gao X, Hao Z, Ma R, Wang P, Shu Y, He J. Crack suppression in laser powder bed fusion of tungsten alloy by using a spherical W-ZrC composite powder. J Alloys Compd 2025;1037:182247. https://doi.org/10.1016/j.jallcom.2025.182247.
[27] Qian B, Zhang J, Liao Z, Chen Y, Wu J, Liao J, et al. Enhanced mechanical properties of Mo–Re alloy via additive manufacturing with gradient transition layer strategy. J Mater Sci Technol 2026;250:62–8. https://doi.org/10.1016/j.jmst.2025.06.028.
[28] Liu H, Sun M, Xia C, Luo X, Zhao C, Wang R, et al. Strength-ductility synergy in TZM alloys achieved via particle-stimulated nucleation and precipitate coherency optimization. Int J Refract Met Hard Mater 2026;134:107427. https://doi.org/10.1016/j.ijrmhm.2025.107427.
[29] Jing K, Zhang C, Liu R, Xie Z-M, Zhang L-C, Zhang L-F, et al. Mechanical properties and thermal shock resistance of tungsten alloys strengthened by laser fragmentation-processed zirconium carbide nanoparticles. Tungsten 2020;2:381–9. https://doi.org/10.1007/s42864-020-00071-5.
[30] Hu W, Wei L, Li Y, Zhang W, Ma Z, Liu C, et al. Phase interface engineering: a new route towards ultrastrong yet ductile Mo alloy. Mater Sci Eng, A 2024;889:145867. https://doi.org/10.1016/j.msea.2023.145867.
[31] Xing H, Hu P, He C, Zhang X, Han J, Yang F, et al. Design of high-performance molybdenum alloys via doping metal oxide and carbide strengthening: a review. J Mater Sci Technol 2023;160:161–80. https://doi.org/10.1016/j.jmst.2023.03.026.
[32] Cui D, Zhao S, Cao Z, Sun C, Dai X, Li C, et al. Differential inhibition of loop and bubble evolution in Ti, Zr and Nb doped Mo-5Re alloy. Acta Mater 2025;294:121149. https://doi.org/10.1016/j.actamat.2025.121149.
[33] Sun L, Li M-J, Chen L, Li Y-H, Qin M-L, Lu G-H, et al. The coordination environment dominated clustering behavior of vacancy and rhenium in molybdenum. Acta Mater 2024;278:120270. https://doi.org/10.1016/j.actamat.2024.120270.
[34] Li Z, Qi C, Cui X, Jia W, Huang S, Zhang Y, et al. In-situ generation of lanthanum oxide for carbide purification in binder jetting W-Ni-Fe alloys. Compos Part A Appl Sci Manuf 2026;205:109679. https://doi.org/10.1016/j.compositesa.2026.109679.
[35] Yuan Y, Yu H, Han Y, Fang W. Synergistic strengthening-toughening strategy for additively manufactured tungsten heavy alloys via alloying element-induced hierarchical microstructures. Chem Eng J 2025;525:170087. https://doi.org/10.1016/j.cej.2025.170087.
[36] Wang X, Zhou W, Wang Y, Gong L, Liu X, Zhou X. MoO_2/Mo heterostructures for hydrogen evolution reaction and ammonia sensing in self-powered mode. Nano Energy 2023;109:108253. https://doi.org/10.1016/j.nanoen.2023.108253.
[37] Yao F, Chen W, Yang Y, Dong L, Elmarakbi A, Fu Y-Q. Unusual ablation behaviors of tungsten graded network reinforced copper composites synthesized by 3D printing and infiltration sintering at ultra-high temperatures. Int J Refract Met Hard Mater 2023;115:106274. https://doi.org/10.1016/j.ijrmhm.2023.106274.
[38] Kim H, Kwon N, Lee Y, Oh S, Park K-T. Removal of inorganic impurities from molten Mo through electron beam melting. Int J Refract Met Hard Mater 2025;128:107036. https://doi.org/10.1016/j.ijrmhm.2025.107036.
[39] Xie Z, Tang Z, Zhang D, Kang Y, Su X, Yang B, et al. Hydrogen arc plasma promotes the purification and nanoparticle preparation of tungsten. Int J Refract Met Hard Mater 2022;105:105815. https://doi.org/10.1016/j.ijrmhm.2022.105815.
[40] Ning L, Tan Y, Wen S, Li P, Cui H, Bai R. Numerical analysis and process optimization of electron beam melting for superalloys. Energy 2024;300:131481. https://doi.org/10.1016/j.energy.2024.131481.
[41] Dash T, Nayak BB. Tungsten carbide – titanium carbide composite preparation by arc plasma melting and its characterization. Ceram Int 2019;45:4771–80. https://doi.org/10.1016/j.ceramint.2018.11.170.
[42] Alkraidi ABN, Mansoor M, Boztemur B, Gökçe H, Kaya F, Yıldırım C, et al. Computational alloy design, synthesis, and characterization of WMoNbVCrx refractory high entropy alloy prepared by vacuum arc melting. J Alloys Compd 2024;1003:175510. https://doi.org/10.1016/j.jallcom.2024.175510.
[43] Wang K, Lv S, Wu H, Wu G, Wang S, Gao J, et al. Recent research progress on the phase-field model of microstructural evolution during metal solidification. Int J Miner Metall Mater 2023;30:2095–111. https://doi.org/10.1007/s12613-023-2710-x.
[44] Zhao Y, Zhang B, Hou H, Chen W, Wang M. Phase-field simulation for the evolution of solid/liquid interface front in directional solidification process. J Mater Sci Technol 2019;35:1044–52. https://doi.org/10.1016/j.jmst.2018.12.009.
[45] Yan X, You X, Yiliti Y, Han W, Dong G, Yang C, et al. The mechanisms for removing O, N, C and metal impurities in the purification of tungsten by electron beam smelting. Sep Purif Technol 2025;376:133893. https://doi.org/10.1016/j.seppur.2025.133893.
[46] Zhang Q, Luo X, Zhu Z, You X, Zhao Z. Purification of molybdenum by electron beam bath smelting. Sep Purif Technol 2025;376:133891. https://doi.org/10.1016/j.seppur.2025.133891.
[47] Tang H, Zhang S, He L, Yang Z, Liu T. 3D printing of high-stiffness and high-strength glass fiber reinforced PEEK composites by selective laser sintering. Compos Part A Appl Sci Manuf 2024;187:108470. https://doi.org/10.1016/j.compositesa.2024.108470.
[48] Lough CS, Liu T, Landers RG, Bristow DA, Drallmeier JA, Brown B, et al. Experiment-based superposition thermal modeling of laser powder bed fusion. Addit Manuf 2025;101:104708. https://doi.org/10.1016/j.addma.2025.104708.
[49] Zhuo L, Liu C, Yin E, Zhao Z, Pang S. Low-cost and low-temperature 3D printing for refractory composite inspired by fused deposition modeling and binder jetting. Compos Part A Appl Sci Manuf 2022;162:107147. https://doi.org/10.1016/j.compositesa.2022.107147.
[50] Di Sturco S, Marchese G, Bondioli F, Lombardi M, Ugues D, Fino P, et al. Understanding the processability, microstructure, and mechanical properties of molybdenum processed by electron beam powder bed fusion. International Int J Refract Met Hard Mater 2025;129:107091. https://doi.org/10.1016/j.ijrmhm.2025.107091.
[51] Johnson JL, Palmer T. Directed energy deposition of molybdenum. Int J Refract Met Hard Mater 2019;84:105029. https://doi.org/10.1016/j.ijrmhm.2019.105029.
[52] Sun Z, Ma Y, Ponge D, Zaefferer S, Jägle EA, Gault B, et al. Thermodynamics-guided alloy and process design for additive manufacturing. Nat Commun 2022;13:4361. https://doi.org/10.1038/s41467-022-31969-y.
[53] Shuai X, Ren J, Yang Y, Shuai Y, Yang M, He C, et al. Atomic scale formation mechanism of laser additively manufactured amorphous-nanocrystalline magnesium alloy. J Alloys Compd 2026;1062:187530. https://doi.org/10.1016/j.jallcom.2026.187530.
[54] Oehlerking F, Stawovy MT, Ohm S, Imandoust A. Microstructural characterization and mechanical properties of additively manufactured molybdenum and molybdenum alloys. Int J Refract Met Hard Mater 2022;109:105971. https://doi.org/10.1016/j.ijrmhm.2022.105971.
[55] Hekmatjou H, Durlov SH, Salehin MN, Ganesh-Ram A, Tanrikulu AA, Ameri N. Layerwise rolling in laser powder bed fusion of tungsten refractory materials: effects and mechanisms. Int J Refract Met Hard Mater 2025;132:107235. https://doi.org/10.1016/j.ijrmhm.2025.107235.
[56] Wang J, Zhao H, Liu Z, Yao D, Li M, Li S, et al. Micro-mechanical analysis on the spreading of tungsten powder in electron beam powder bed fusion additive manufacturing. Particuology 2025;105:277–87. https://doi.org/10.1016/j.partic.2025.08.008.
[57] Islam S, Seo G-J, Ahsan MRU, Villarraga-Gómez H, Lee H-J, Kim DB. Investigation of microstructures, defects, and mechanical properties of titanium-zirconium-molybdenum alloy manufactured by wire arc additive manufacturing. Int J Refract Met Hard Mater 2023;110:106042. https://doi.org/10.1016/j.ijrmhm.2022.106042.
[58] Heng Y, Mao Y, Feng K, Zheng J, Xie Y, Wei Q. Enhanced density and fine W particles of W-7Ni-3Fe alloys prepared by binder jetting additive manufacturing with a two-step sintering strategy. Int J Refract Met Hard Mater 2025;128:107037. https://doi.org/10.1016/j.ijrmhm.2025.107037.
[59] Li X, Wang Q, Wei S, Lou W, Liang J, Chen L, et al. Microstructure and high-temperature mechanical properties of Cu-W composite prepared by hot isostatic pressing. J Alloys Compd 2024;970:172571. https://doi.org/10.1016/j.jallcom.2023.172571.
[60] Niu Y, Fu S, Zhang K, Dai B, Zhang H, Grasso S, et al. Synthesis, microstructure, and properties of high purity Mo_2TiAlC_2 ceramics fabricated by spark plasma sintering. J Adv Ceram 2020;9:759–68. https://doi.org/10.1007/s40145-020-0412-7.

[61] Zhang L, Li X, Qu X, Qin M, Que Z, Wei Z, et al. Powder metallurgy route to ultrafine-grained refractory metals. Adv Mater 2023;35:2205807. https://doi.org/10.1002/adma.202205807.

[62] Aslan M, Çakır MV, Elmossa A. Effects of a novel tungsten alloy(W-Mn-Cu-Sn) particles, produced through powder metallurgy, on the mechanical and failure characterization of adhesively single-lap bonded GFRP joints. Int J Adhes Adhes 2025;141:104043. https://doi.org/10.1016/j.ijadhadh.2025.104043.

[63] Hu W, Sun T, Liu C, Yu L, Ahamad T, Ma Z. Refined microstructure and enhanced mechanical properties in Mo-Y_2O_3 alloys prepared by freeze-drying method and subsequent low temperature sintering. J Mater Sci Technol 2021;88:36–44. https://doi.org/10.1016/j.jmst.2021.01.064.

[64] Dong Z, Liu N, Hu W, Ma Z, Li C, Liu C, et al. Controlled synthesis of high-quality W-Y_2O_3 composite powder precursor by ascertaining the synthesis mechanism behind the wet chemical method. J Mater Sci Technol 2020;36:118–27. https://doi.org/10.1016/j.jmst.2019.05.067.

[65] Reszczyńska J, Grzyb T, Wei Z, Klein M, Kowalska E, Ohtani B, et al. Photocatalytic activity and luminescence properties of RE^{3+}–TiO_2 nanocrystals prepared by sol–gel and hydrothermal methods. Appl Catal B Environ 2016;181:825–37. https://doi.org/10.1016/j.apcatb.2015.09.001.

[66] Wei Y, Yang H-L, Tao L-Z, Gui K-X, Luo L-M. Research progress and development of strengthening-toughening methods for molybdenum alloys prepared by powder metallurgy. J Alloys Compd 2025;1010:177099. https://doi.org/10.1016/j.jallcom.2024.177099.

[67] Wang J, Dong H, Xu H, Fan F, Xu H, Wu H, et al. Effect of powder size on the moldability and pore characteristics of porous tungsten by injection molding. Powder Technol 2025;452:120472. https://doi.org/10.1016/j.powtec.2024.120472.

[68] Rednyk A, Matějíček J, Vilémová M, Veverka J, Klečka J, Lukáč F, et al. Enhanced tungsten densification via modified field-assisted sintering. Mater Today Commun 2025;46:112939. https://doi.org/10.1016/j.mtcomm.2025.112939.

[69] Seikh Z, Sekh M, Mandal G, Sengupta B, Sinha A. Metal matrix composites processed through powder metallurgy: a brief overview. J Inst Eng India Ser D 2025;106:771–8. https://doi.org/10.1007/s40033-024-00651-6.

[70] Singh I, Dabhade VV. A prospective into rapid consolidation of W-Ni-Fe based tungsten heavy alloys with the addition of Nb and Mo aided by spark plasma sintering. J Alloys Compd 2025;1044:184338. https://doi.org/10.1016/j.jallcom.2025.184338.

[71] Shen C, Le J, Chen F, Ye Y, Zhang J, Zhuo Y, et al. Achieving strength-ductility synergy of (TiB + TiC)/Ti-6Al-4V composites by HIP via promoting <c+a> dislocation activity and slip transmission. Compos Part A Appl Sci Manuf 2026;208:109889. https://doi.org/10.1016/j.compositesa.2026.109889.

[72] Wang J, Liu W, Ma Y, Zhu W, Chen B, Zhang L, et al. Research on hot isostatic pressing sintering behavior of 90W–Ni–Fe–Cu alloy. J Mater Res Technol 2023;26:7284–99. https://doi.org/10.1016/j.jmrt.2023.09.053.

[73] Dudina DV, Georgarakis K, Olevsky EA. Progress in aluminium and magnesium matrix composites obtained by spark plasma, microwave and induction sintering. Int Mater Rev 2023;68:225–46. https://doi.org/10.1080/09506608.2022.2077029.

[74] Zou Q, Wu D, Yu X, Li M, An X, Jie J. Elaborating Cu-network structure of W@20Cu composites with Cu-coated W powders via oscillating pressure sintering. J Alloys Compd 2025;1014:178629. https://doi.org/10.1016/j.jallcom.2025.178629.

[75] Chen P, Huang C, Su J, Xu D, Chen H, Shen X, et al. Temperature difference-induced surface tension gradients enable high densification of W-30Cu composites via ultrafast high-temperature sintering. J Mater Res Technol 2025;39:862–72. https://doi.org/10.1016/j.jmrt.2025.09.171.

[76] Ruset C, Grigore E, Maier H, Neu R, Greuner H, Mayer M, et al. Development of W coatings for fusion applications. Fusion Eng Des 2011;86:1677–80. https://doi.org/10.1016/j.fusengdes.2011.04.031.

[77] Kim H, Lee HJ, Jang C. Thermal performance of multilayer PVD tungsten coating for the first wall application in nuclear fusion devices. Fusion Sci Technol 2015;68:378–82. https://doi.org/10.13182/fst14-958.

[78] Ahmed N, Khan ZS, Ali A. Microstructure and residual stress dependence of molybdenum films on DC magnetron sputtering conditions. Appl Phys A 2022;128:967. https://doi.org/10.1007/s00339-022-06097-5.

[79] Zhou Q, Jiao Z, Huang Z, Shi Y, Li Y, Yin C, et al. Wear-resistant CrCoNi nanocrystalline film via friction-driven surface segregation. Acta Mater 2024;279:120299. https://doi.org/10.1016/j.actamat.2024.120299.

[80] Jorg T, Music D, Hauser F, Cordill MJ, Franz R, Kostenbauer H, et al. Deformation behavior of re alloyed mo thin films on flexible substrates: in situ fragmentation analysis supported by first-principles calculations. Sci Rep 2017;7:7374. https://doi.org/10.1038/s41598-017-07825-1.

[81] Maier H, Rasinski M, Grigore E, Ruset C, Greuner H, Böswirth B, et al. Performance of W coatings on CFC with respect to carbide formation. J Nucl Mater 2011;415:S310–2. https://doi.org/10.1016/j.jnucmat.2010.08.049.

[82] Ruset C, Grigore E, Falie D, Gherendi M, Maier H, Rasinski M, et al. The impact of thermal fatigue and carbidization on the w coatings deposited on cfc tiles for the iter-like wall project at jet. Fusion Eng Des 2013;88:1690–3. https://doi.org/10.1016/j.fusengdes.2013.02.017.

[83] Rao SI, Woodward C, Akdim B, Senkov ON, Miracle D. Theory of solid solution strengthening of BCC chemically complex alloys. Acta Mater 2021;209:116758. https://doi.org/10.1016/j.actamat.2021.116758.

[84] Madec R, Kubin LP. Dislocation strengthening in FCC metals and in BCC metals at high temperatures. Acta Mater 2017;126:166–73. https://doi.org/10.1016/j.actamat.2016.12.040.

[85] Sun BZ, Gao L, Lou LH, Li R, Song JP, Liu YL, et al. Microstructure and mechanical properties of W-HfC alloy synthesized by in-situ fabrication via pressureless sintering. Int J Refract Met Hard Mater 2025;127:106978. https://doi.org/10.1016/j.ijrmhm.2024.106978.

[86] Hu H, Zhang C, Yue R, Hu B, Chen S. Unraveling ductility enhancement mechanisms in W-Ta alloys using machine-learning potential. Int J Mech Sci 2025;286:109911. https://doi.org/10.1016/j.ijmecsci.2024.109911.

[87] Zhang C, Wang P, Liu CY, Liu ZY, Wu MW, Gao XH, et al. A novel crack-free Ti-modified Mo alloy designed for laser powder bed fusion. J Alloys Compd 2022;910:164802. https://doi.org/10.1016/j.jallcom.2022.164802.

[88] Liu W, Huang Y, Wang Y, Liu W, Ma Y. W–Ta–Nb solid solutions prepared by vacuum arc melting: microstructure evolution and mechanical properties. Vacuum 2023;212:111959. https://doi.org/10.1016/j.vacuum.2023.111959.

[89] Liu J, Huang Y, Liu W, Wang Y, Zhang Y, Ma Y. Effect of tantalum concentration on the microstructure and mechanical properties of novel W–Ta-Re alloy. Vacuum 2023;207:111627. https://doi.org/10.1016/j.vacuum.2022.111627.

[90] Yang Q, Hua X, Quan C, Wang H, Wang L, Xing H, et al. Enhanced mechanical properties and thermal stability of boron doped molybdenum alloy. Int J Refract Met Hard Mater 2025;133:107354. https://doi.org/10.1016/j.ijrmhm.2025.107354.

[91] Conklin DR, Klein-Hessling Barrientos HF, Croell A, Rosales J, Warren KJ, Weimer AW. Preparation of homogeneous W Re alloys by coating tungsten powder with perrhenic acid. Int J Refract Met Hard Mater 2025;132:107285. https://doi.org/10.1016/j.ijrmhm.2025.107285.

[92] Xu L, Li N, Song W, Sun T, Zhou Y, Wei S, et al. Achieving an unprecedented strength-ductility balance of molybdenum alloy by homogeneously distributing yttrium-cerium oxide. J Alloys Compd 2022;897:163110. https://doi.org/10.1016/j.jallcom.2021.163110.

[93] Xiao F, Barriere T, Cheng G, Miao Q, Zuo S, Wei S, et al. Extremely uniform nanosized oxide particles dispersion strengthened tungsten alloy with high tensile and compressive strengths fabricated involving liquid. J Alloys Compd 2021;878:160335. https://doi.org/10.1016/j.jallcom.2021.160335.

[94] Yang J, Chen Z, Yu Y, Xu H, Jia B, Wu H, et al. The effect of La_2O_3 content on the microstructure and mechanical properties of W-La_2O_3 alloys via pressureless sintering. Mater Charact 2025;227:115239. https://doi.org/10.1016/j.matchar.2025.115239.

[95] Guo C, Li X, Mei E, Liu J, Xu H, Chao Y, et al. Low-temperature sintering of W-HfC core-shell powders for microstructure regulation. Int J Refract Met Hard Mater 2026;137:107676. https://doi.org/10.1016/j.ijrmhm.2026.107676.

[96] Li X, Shi H, Wang X, Hu X, Xu C, Shao W. Achieving high strength and ductility in GNSs/Mg nanocomposites fabricated by in-situ liquid metallurgy combined with hot extrusion. Compos Part A Appl Sci Manuf 2022;161:107079. https://doi.org/10.1016/j.compositesa.2022.107079.

[97] Zhang Y, Yang Z, Pan T, Gao H, Guan H, Xu J, et al. Construction of natural fiber/polyaniline core-shell heterostructures with tunable and excellent electromagnetic shielding capability via a facile secondary doping strategy. Compos Part A Appl Sci Manuf 2020;137:105994. https://doi.org/10.1016/j.compositesa.2020.105994.

[98] Lang ST, Yan QZ, Sun NB, Zhang XX. Preparation of W–TiC alloys from core–shell structure powders synthesized by an improved wet chemical method. Rare Met 2023;42:1378–86. https://doi.org/10.1007/s12598-018-1066-2.

[99] Hu P, Gong X, Liu H, Zhou W, Wang J. A novel dissolution-precipitation strategy to accelerate the sintering of yttrium oxide dispersion strengthened tungsten alloy with well-regulated structure. J Mater Sci Technol 2024;184:43–53. https://doi.org/10.1016/j.jmst.2023.11.004.

[100] Jing K, Liu R, Xie ZM, Ke JG, Wang XP, Fang QF, et al. Excellent high-temperature strength and ductility of the ZrC nanoparticles dispersed molybdenum. Acta Mater 2022;227:117725. https://doi.org/10.1016/j.actamat.2022.117725.

[101] Yao L, Gao Y, Li Y, Huang X, Wang Y, Huang Y. Preparation of nanostructural oxide dispersion strengthened (ODS) Mo alloy by mechanical alloying and spark plasma sintering, and its characterization. Int J Refract Met Hard Mater 2022;105:105822. https://doi.org/10.1016/j.ijrmhm.2022.105822.

[102] Zhu Y, Wu X. Heterostructured materials. Prog Mater Sci 2023;131:101019. https://doi.org/10.1016/j.pmatsci.2022.101019.

[103] Gaitzsch U, Magnusson A, Weißgärber T. MoSiBTi by powder metallurgy. Int J Refract Met Hard Mater 2023;112:106127. https://doi.org/10.1016/j.ijrmhm.2023.106127.

[104] Wei Z, Lin K, Wang X, Zhao Y-P. Peeling of graphene/molybdenum disulfide heterostructure at different angles: a continuum model with accommodations for van der waals interaction. Compos Part A Appl Sci Manuf 2021;150:106592. https://doi.org/10.1016/j.compositesa.2021.106592.

[105] Romankov S, Park YC, Shchetinin IV. Fabrication of W and Mo layers with multi-modal structures on Ti sheets through intense plastic deformation induced by ball collisions. Surf Coat Technol 2019;357:473–82. https://doi.org/10.1016/j.surfcoat.2018.10.040.

[106] Chou TH, Li WP, Chang HW, Du XH, Chuang WS, Yang T, et al. Quantitative analysis of hetero-deformation induced strengthening in heterogeneous grain structure. Int J Plast 2022;159:103482. https://doi.org/10.1016/j.ijplas.2022.103482.

[107] Ning H, Nie Z, Hao Y, Yu X, Tan C. Improved fracture behavior and microstructural characterization of heterogeneous-structured tungsten. Mater Sci Eng, A 2021;805:140813. https://doi.org/10.1016/j.msea.2021.140813.

[108] Li S, Chen F, Li Z, Xiao S, Wang M, Wei Z, et al. Achieving exceptional strength-ductility synergy in titanium matrix composites via controllable bimodal grain structure and configuration of nano-reinforcements. Compos Part A Appl Sci Manuf 2026;202:109454. https://doi.org/10.1016/j.compositesa.2025.109454.

[109] Jia Z, Zhang Y, Jin J, Sun H, Zhao Z, Lu W, et al. Multiphase-synergistic regulation strategy achieving superior strength-plasticity and prolonged strain-hardening of (Ti, Nb)B-reinforced Ti2AlNb composite. Compos Part A Appl Sci Manuf 2026; 200:109351. https://doi.org/10.1016/j.compositesa.2025.109351.
[110] Li L, Dong Z, Ma Z, Liu C, Yu L, Liu Y. Ultrahigh strength and toughness in W-Y_2O_3 alloy with bimodal and lamellar structures. Mater Res Lett 2023;11:439–45. https://doi.org/10.1080/21663831.2023.2181110.
[111] Hu Y, Xu A, Liu J, Wang R, Suo J. Enhancing the strength and toughness of WTaTiVN+Taμm heterogeneous alloys via nano Ti–V–N precipitation phase adjustment. J Mater Res Technol 2025;35:2934–45. https://doi.org/10.1016/j.jmrt.2025.01.212.
[112] Awasthi PD, Dhal A, Michael FN, Mishra RS. Near crack free additive manufacturing of a novel W-Nb-C alloy. Mater Res Lett 2025;13:67–75. https://doi.org/10.1080/21663831.2024.2419475.
[113] Lin C, Lu H, Ren X, He B, Peng X, Chen P. Long-term efficient electrosynthesis of adipic acid and hydrogen by heterostructural molybdenum-nickel alloy electrode. Chem Eng J 2025;509:161475. https://doi.org/10.1016/j.cej.2025.161475.
[114] Ren Y, Zhu L, Li Y, Zhou Q, Eder SJ, Sui X, et al. Cryogenic tribological breakthroughs in medium-entropy alloy composites via regulated partial recrystallization. Sci China Mater 2026;69:4896–911. https://doi.org/10.1007/s40843-025-4018-6.
[115] Xie J, Li H, Li F, Shi P. Multilayer heterostructure inhomogeneous model for the functionally graded spherical shell with rotation effect for arbitrarily varying material properties. Compos Struct 2024;339:118145. https://doi.org/10.1016/j.compstruct.2024.118145.
[116] Wu Y, Gu X, Jia M, Shen Q, Chen F. Enhanced joining of silicon nitride and molybdenum via functionally graded structures: reaction mechanism and microstructural optimization. Ceram Int 2025;51:43691–700. https://doi.org/10.1016/j.ceramint.2025.07.100.
[117] Chen F, Jia M, She Y, Wu Y, Shen Q, Zhang L. Mechanical behavior of AlN/Mo functionally graded materials with various compositional structures. J Alloys Compd 2020;816:152512. https://doi.org/10.1016/j.jallcom.2019.152512.
[118] Jia M, Chen F, Wu Y, Xu L, Shen Q, Jiang N, et al. Microstructure and shear fracture behavior of Mo/AlN/Mo symmetrical compositionally graded materials. Mater Sci Eng, A 2022;834:142591. https://doi.org/10.1016/j.msea.2021.142591.
[119] Zhu J, Cao S, Liu H. Fabrication of W–Ni–Fe alloys with gradient structures. Int J Refract Met Hard Mater 2013;36:72–5. https://doi.org/10.1016/j.ijrmhm.2012.03.017.
[120] Dong LL, Ahangarkani M, Zhang W, Zhang B, Chen WG, Fu YQ, et al. Formation of gradient microstructure and mechanical properties of hot-pressed W-20 wt% Cu composites after sliding friction severe deformation. Mater Charact 2018;144:325–35. https://doi.org/10.1016/j.matchar.2018.07.016.
[121] Zhang Q, Liang S, Zhuo L. Fabrication and properties of the W-30wt%Cu gradient composite with W@WC core-shell structure. J Alloys Compd 2017;708:796–803. https://doi.org/10.1016/j.jallcom.2017.03.064.
[122] Deng N, Li J, Wang Y, Qu D, Zhang K, Zhou Z. Microstructure and mechanical properties of liquid–phase sintered W@NiFe composite powders. Int J Refract Met Hard Mater 2021;95:105447. https://doi.org/10.1016/j.ijrmhm.2020.105447.
[123] Zhang Q, Chen B, Chen Z, Zhu Z, Hu X, Ding Y, et al. Microstructure and properties of W Cu composites reinforced by in-situ generated WC. Int J Refract Met Hard Mater 2021;99:105585. https://doi.org/10.1016/j.ijrmhm.2021.105585.
[124] Ji Y, Zhang L, Lu X, Fu H, Zhu Z, Li H, et al. Microstructure and tensile properties of Co-free Fe4CrNi(AlTi) high-entropy alloys. Intermetallics 2021;138:107339. https://doi.org/10.1016/j.intermet.2021.107339.
[125] Zhang L, Chen X, Huang Y, Liu W, Ma Y. Microstructural characteristics and evolution mechanisms of 90W–Ni–Fe alloy under high-strain-rate deformation. Mater Sci Eng, A 2021;811:141070. https://doi.org/10.1016/j.msea.2021.141070.
[126] Shakunt NS, Gouthama Upadhyaya A. Effect of La_2O_3 addition on microstructure and mechanical properties of W-Ni-Cu tungsten heavy alloy. Mater Chem Phys 2024;318:129227. https://doi.org/10.1016/j.matchemphys.2024.129227.
[127] Han Y, Li Y, Ye L, Du Z, Liu Z, Li X, et al. A novel dissolution-precipitation mechanism during liquid phase sintering and its strengthening effects in W-Ni-Fe alloys with low W contents. Mater Des 2022;220:110841. https://doi.org/10.1016/j.matdes.2022.110841.
[128] R M, A RA. Crystallographic texture evolution in hot-press sintered tungsten heavy alloy with the effect of niobium (Nb) addition. Mater Today Commun 2024;39:108971. https://doi.org/10.1016/j.mtcomm.2024.108971.
[129] Singh I, Dabhade V, Debata M, Panigrahi A. The role of addition of Mo and Nb on microstructure, phase and mechanical properties in tungsten heavy alloys. J Alloys Compd 2025;1010:177466. https://doi.org/10.1016/j.jallcom.2024.177466.
[130] Seifert U. From stochastic thermodynamics to thermodynamic inference. Annu Rev Condens Matter Phys 2019;10:171–92. https://doi.org/10.1146/annurev-conmatphys-031218-013554.
[131] Blaschke DN, Hunter A, Preston DL. Phase transformation kinetics model for metals. Int J Plast 2026;196:104579. https://doi.org/10.1016/j.ijplas.2025.104579.
[132] Xu Z, Xu L, Xiong N, Yao Y, Li X, Wei S. Dynamic recrystallization behavior of a Mo-2.0%ZrO_2 alloy during hot deformation. Int J Refract Met Hard Mater 2022; 109:105983. https://doi.org/10.1016/j.ijrmhm.2022.105983.
[133] Huang L, Yang Y, Liang J, Lin X, Gao X, Li Y, et al. Microstructural evolutions of molybdenum-rhenium (47.5 wt.%) alloy under room and high temperature compressions. Mater Charact 2024;212:114001. https://doi.org/10.1016/j.matchar.2024.114001.
[134] Ma S, Dong D, Zhang M, Gao Y, Wu Z, Wang D. Tensile behavior and microstructure evolution of Mo-14 %Re alloy at room temperature and elevated temperatures. Int J Refract Met Hard Mater 2025;128:106996. https://doi.org/10.1016/j.ijrmhm.2024.106996.
[135] Wei Y, Ma M, Zhang S, Hu Y, Li Q, Zhu L. Investigation of the microstructure and properties of a ZrC-reinforced TZM molybdenum alloy. Int J Refract Met Hard Mater 2025;131:107188. https://doi.org/10.1016/j.ijrmhm.2025.107188.
[136] Yang L, Zheng XY, Zhao Y, Wang XR, Xiao FN, Wei SZ. Dynamic recrystallization behavior and strengthening mechanism of a novel Mo–Ti_3AlC_2 alloy at ultrahigh temperature. Rare Met 2024;43:3946–60. https://doi.org/10.1007/s12598-024-02669-x.
[137] Yang Q, Hua X, Quan C, Wang H, Wang L, Xing H, et al. Microstructure evolution and strengthening mechanism of boron doped molybdenum alloy solid solution rolled plates. J Alloys Compd 2025;1035:181568. https://doi.org/10.1016/j.jallcom.2025.181568.
[138] Li SL, Hu P, Xing HR, Wang H, Zhang W, Yu L, et al. Solute-induced precipitation nanosized Ti-rich phase greatly enhances the plasticity of Mo-Ti-Zr alloys. Mater Des 2026;261:115279. https://doi.org/10.1016/j.matdes.2025.115279.
[139] Yang J, Wang S, Wang K, Fang Y, Wang H, Wang L, et al. Molybdenum-rhenium alloy: a focused review of strengthening-toughening mechanism and method. Int J Refract Met Hard Mater 2026;134:107408. https://doi.org/10.1016/j.ijrmhm.2025.107408.
[140] Zheng Z, Lai C, Zhou W, Wang Y, Zhang Y, Wang J. Preparation, mechanical properties and strengthening mechanism of W-Re alloys: a review. Materials 2023;17:102. https://doi.org/10.3390/ma17010102.
[141] Yin Y, Wang T, Qin S, Wang W, Shi Y, Yu H. Research on microstructure, mechanical properties, and high-temperature stability of hot-rolled tungsten hafnium alloy. Materials 2024;17:3633. https://doi.org/10.3390/ma17153663.
[142] Zhou J, Sun J, Zhang L, Chen B, Wang J, Ma Y, et al. Dynamic recrystallization induced adiabatic shear failure of dual-phase 93W-4.9Ni-2.1Fe alloy during high-speed dynamic loading. Mater Charact 2025;224:115063. https://doi.org/10.1016/j.matchar.2025.115063.
[143] Wang X, Jiao A, Zhu Y, Guo Y, Xue K, Li P. Microstructure evolution and microhardness improvement of tantalum-modified tungsten heavy alloy processed by high-pressure torsion processing. Int J Refract Met Hard Mater 2025; 133:107388. https://doi.org/10.1016/j.ijrmhm.2025.107388.
[144] Gao Z, Liu Z, Mao X, Duan G, Chen J. Influence of scanning speed on composition, density, microstructure, and mechanical properties of SLM high-density W-Ni-Fe alloys. J Alloys Compd 2026;1054:186339. https://doi.org/10.1016/j.jallcom.2026.186339.
[145] Cunningham WS, Lang E, Sprouster D, Olynik N, Pattammattel A, Olds D, et al. Alloying effects on the microstructure and properties of laser additively manufactured tungsten materials. Mater Sci Eng, A 2024;914:147110. https://doi.org/10.1016/j.msea.2024.147110.
[146] Hao Z, Zhao Z, Zhang G, Zhang S, Li Z, Yao B, et al. Microstructure evolution and mechanical properties of tungsten alloy prepared by laser directed energy deposition. J Alloys Compd 2025;1010:177056. https://doi.org/10.1016/j.jallcom.2024.177056.
[147] Zhou X, Wei S, Li Z, Yang L, Wang X, Liu S, et al. Microstructure and properties of tungsten heavy alloys reinforced with ZrO_2 particles by spark plasma sintering. Int J Refract Met Hard Mater 2025;132:107277. https://doi.org/10.1016/j.ijrmhm.2025.107277.
[148] Dai Y, Li K, Zou J, Luo X, Zhang G, Shi M, et al. Effect of quenching temperature on the microstructure evolutions and strength-ductility of W-Ni-Cu alloy at room-temperature and cryogenic. Int J Refract Met Hard Mater 2024;122:106697. https://doi.org/10.1016/j.ijrmhm.2024.106697.
[149] Hu Z, Zhao Y, Zhan X, Xu J, Ma Z. The immiscible W/Cu composites with heterostructures and excellent bond strength prepared by additively manufactured transient liquid-phase direct bonding: experiments and simulations. Compos Part B Eng 2025;291:111981. https://doi.org/10.1016/j.compositesb.2024.111981.
[150] Lv Y, Zhao S, Han Y, Cheng H, Ye Z, Zhang H, et al. The microstructure and radiation resistance of fine-grained W-0.3 wt%Y_2O_3 prepared by nano in-situ composite exposed to low-energy and high-flux helium plasma. J Alloys Compd 2022;903:163927. https://doi.org/10.1016/j.jallcom.2022.163927.
[151] Xu D, Chen P, Fu K, Sang C, Chen R, Hong T, et al. Connection reinforcement design of ODS-W/Cu joint: transforming immiscible interface into dual reaction diffusion interface. Mater Charact 2025;228:115402. https://doi.org/10.1016/j.matchar.2025.115402.
[152] Xu G, Yan Z, Lu H, Cai J, Wang R, Feng F, et al. Thermal shock resistance and toughening mechanism of W/Ta and W/TiN/Ta laminated composites. Int J Refract Met Hard Mater 2022;105:105810. https://doi.org/10.1016/j.ijrmhm.2022.105810.
[153] Chu Q, Xing H, Yang Z, Wang H, Fang Y, Xu L, et al. Enhanced strength of a novel La-TZM alloy via multicomponent second phase strengthening mechanism. Mater Charact 2025;228:115433. https://doi.org/10.1016/j.matchar.2025.115433.
[154] Mu Y, Shen C, Li Z, Shi S, Xiong L. Effect of process parameters on microstructure and properties of W-Ti-Zr-Nb tungsten alloy fabricated by LPBF. Int J Refract Met Hard Mater 2025;126:106945. https://doi.org/10.1016/j.ijrmhm.2024.106945.
[155] Hu W, He J, Yang Z, Tan J, Chen S, Liu S, et al. Strengthening the grain boundary of Mo alloy via little TiC addition. Mater Charact 2023;203:113063. https://doi.org/10.1016/j.matchar.2023.113063.
[156] Li S-L, Hu P, Liu T, Shi Q-S, Dang X-M, Hu B-L, et al. Formation mechanism of coronal composite secondary phase in titanium-zirconium-molybdenum alloy.

Mater Charact 2022;193:112235. https://doi.org/10.1016/j.matchar.2022.112235.
[157] Fan F, Wang J, Xu H, Liu S, Song H, Chen Q, et al. Balancing mechanical properties in tungsten-alumina oxide alloys via coherent/semi-coherent interfaces. Compos Part B Eng 2025;295:112204. https://doi.org/10.1016/j.compositesb.2025.112204.
[158] Xie XF, Zhang Y, Xie ZM, Cheng X, Liu R, Fang QF, et al. Stable nanoparticles dispersion induced an unprecedented high strength in a bulk W-TiC alloy. Scr Mater 2023;224:115136. https://doi.org/10.1016/j.scriptamat.2022.115136.
[159] Wang J, Huang Y, Wang Y, Zhou J, Fan P, Li Z, et al. Superior strength-ductility synergy in a novel Co addition tailored W-Ta-Ni-Fe composite. J Alloys Compd 2025;1045:184756. https://doi.org/10.1016/j.jallcom.2025.184756.
[160] Li X, Liu H, Hu P, Wang J, Yang Y, Li H, et al. Nanostructured TiC dispersion-strengthened tungsten composite with remarkably improved He ion irradiation resistance. Int J Refract Met Hard Mater 2022;107:105900. https://doi.org/10.1016/j.ijrmhm.2022.105900.
[161] Ji C-C, Li Z-B, Xi Y-T, Ren Z-W, Li M-Y, Sun G-D. Unveiling the effect of Ti_3O_5 nanoparticles on the microstructure elevation and mechanical properties of ultrafine-grained Mo composites. Mater Sci Eng, A 2025;928:148078. https://doi.org/10.1016/j.msea.2025.148078.
[162] Wang Y, Huang Y, Liu W, Chen B, Liu J, Zhang L, et al. Investigation of diffusion reaction mechanism between W20Ta solid solution and Ni. Mater Charact 2023;200:112894. https://doi.org/10.1016/j.matchar.2023.112894.
[163] Wang Y, Huang Y, Liu W, Chen B, Liu J, Zhang L, et al. In-situ formation of Ni_3Ta nanophase for strengthening tungsten alloy. J Alloys Compd 2023;941:168927. https://doi.org/10.1016/j.jallcom.2023.168927.
[164] Zhang X, Xia Y, Ma L, Li Y, Chen X, Ding X, et al. Achieving high strength in BNNSs reinforced W-Re alloys via heterogeneous particles with coherent interface. Mater Sci Eng, A 2026;949:149431. https://doi.org/10.1016/j.msea.2025.149431.
[165] Mao R, Xiang D. Improving mechanical properties of W-Ni_3Al alloy through Zr element addition: Solid-solution and oxide particle strengthening. J Alloys Compd 2024;1002:175240. https://doi.org/10.1016/j.jallcom.2024.175240.
[166] Ning Z, Li X, Wei S, Liang J, Wu J, Zhang X, et al. Effect of alloying elements (Ni, Co, Cr, and Sn) on the mechanical properties of W–Cu alloy system predicted from first principles. J Mater Sci 2024;59:18776–93. https://doi.org/10.1007/s10853-024-10300-8.
[167] Li S, Li J, Zhou Q, Liang Z, Wang T, Eder SJ, et al. Graphene interfaces regulate fracture in metallic glass based composites. Int J Mech Sci 2026;326:111865. https://doi.org/10.1016/j.ijmecsci.2026.111865.
[168] Zhang Y-H, Ma E, Sun J, Han W-Z. Unveiling the intrinsic rhenium effect in tungsten. Acta Mater 2024;264:119586. https://doi.org/10.1016/j.actamat.2023.119586.
[169] Feng Z, Yang L, Li B, Ma Y, Li D, Zhu J, et al. Unraveling the solid solution effects of rhenium and tantalum alloying on the strength and ductility of tungsten single crystals. J Alloys Compd 2026;1050:185573. https://doi.org/10.1016/j.jallcom.2025.185573.
[170] Fan P, Huang Y, Liu J, Liu W, Wang Y, Ma Y. Preparation of high strength and tough fine grained W-Ta-Re alloy via high energy ball milling and spark plasma sintering. J Alloys Compd 2025;1037:182651. https://doi.org/10.1016/j.jallcom.2025.182651.
[171] Zhang X, Li H, Xu Y, Liu Q, Liu Y, Cui Z, et al. First-principles study on the mechanical properties and thermodynamic properties of Mo–Ta alloys. Plasma Sci Technol 2020;22:065601. https://doi.org/10.1088/2058-6272/ab78bc.
[172] Zhao Y, Chen L, Guo H, Tang J, Kong X, Guan Y. Dislocation-graphene interactions and strengthening mechanisms in aluminum matrix composites: from orowan mechanism to cross-slip. Compos Part A Appl Sci Manuf 2026;204:109668. https://doi.org/10.1016/j.compositesa.2026.109668.
[173] Li J, Zhou M, Yang J, Mou Y, Wang J, Zhu S, et al. Multiscale toughening-driven lattice-structured titanium matrix composites: Breakthrough in strength-toughness synergy. Compos Part A Appl Sci Manuf 2026;202:109463. https://doi.org/10.1016/j.compositesa.2025.109463.
[174] Chen Y, Fang Y, Cheng P, Ke X, Zhang M, Zou J, et al. The origin of exceptionally large ductility in molybdenum alloys dispersed with irregular-shaped La_2O_3 nano-particles. Nat Commun 2024;15:4105. https://doi.org/10.1038/s41467-024-48439-2.
[175] Cheng X, Xie Z-M, Xie X-F, Zeng L-F, Liu R, Yang J-F, et al. Achieving a remarkable low-temperature tensile ductility in a high-strength tungsten alloy. Tungsten 2023;6:150–61. https://doi.org/10.1007/s42864-023-00218-0.
[176] Liu S, Li Z, Zhou X, Yang L, Xu L, Wang X, et al. Effect of heat treatment and rotary swaging on microstructure and mechanical properties of 91W–Ni–Fe–Co alloy. J Mater Res Technol 2025;37:3869–79. https://doi.org/10.1016/j.jmrt.2025.07.077.
[177] Ma S, Dong D, Gao Y, Zhang M, Wu Z, Wang D. Tensile creep deformation behavior of Mo-14 %Re alloy at elevated temperature. Mater Sci Eng, A 2025;946:149114. https://doi.org/10.1016/j.msea.2025.149114.
[178] Li Z, Jiao B, Zhang W, Yin T, Hu Z, Zhang W, et al. Unveiling the superior high-temperature mechanical property of molybdenum single crystal by adding Nb element. Int J Refract Met Hard Mater 2026;134:107407. https://doi.org/10.1016/j.ijrmhm.2025.107407.
[179] Fan Z, Gao F, Wang Y, Men H, Zhou L. Effect of solutes on grain refinement. Prog Mater Sci 2022;123:100809. https://doi.org/10.1016/j.pmatsci.2021.100809.
[180] Chen B, Li Z-B, Liu J-R, Zhang G-H. Effect of molybdenum addition on microstructure and mechanical properties of 90% tungsten heavy alloys. Int J Refract Met Hard Mater 2022;106:105868. https://doi.org/10.1016/j.ijrmhm.2022.105868.
[181] Shi T-K, Guo L-F, Zhou K, Li Z-B, Li Y. Enhancing strength-ductility synergy by introducing Nb micro-alloying in W-Ni-Fe alloys fabricated via powder metallurgy technique. Int J Refract Met Hard Mater 2025;132:107278. https://doi.org/10.1016/j.ijrmhm.2025.107278.
[182] Zhang G, Chen G, Panwisawas C, Teng X, Ma Y, An R, et al. First-principles study of oxygen segregation and its effect on the embrittlement of molybdenum symmetrical tilt grain boundaries. Acta Mater 2023;261:119387. https://doi.org/10.1016/j.actamat.2023.119387.
[183] Liu R, Zhao W, Tian Y, Zhang J, Luo G, Shen Q. The synergetic effect of TaC particles and Re alloy on microstructure and mechanical properties in tungsten alloy. J Mater Res Technol 2024;28:4639–46. https://doi.org/10.1016/j.jmrt.2024.01.035.
[184] Chen S, Wang X, Jiang Z, Yang J, Ye Z, Wang W, et al. AlN reinforced Fe activated sintered tungsten matrix composites: mechanical properties, fracture behaviors and reinforcement mechanisms. J Alloys Compd 2024;1004:175815. https://doi.org/10.1016/j.jallcom.2024.175815.
[185] Dai Y, Li K, Luo X, Zhang G, Pan W, Wang G, et al. Mn-regulated nano-amorphous bands facilitate strength-ductility synergy in W-NiFeCoMn alloys. Mater Sci Eng, A 2025;947:149197. https://doi.org/10.1016/j.msea.2025.149197.
[186] Zhang W, Chen W, Li Y, He X, Zhou Z. Achieving synergistic strength-ductility enhancement of HfC fine-particle dispersed molybdenum alloy. J Alloys Compd 2025;1027:180600. https://doi.org/10.1016/j.jallcom.2025.180600.
[187] Zhao Z, Sun T, Wang C, Yu H, Cui L, Dou C, et al. Mechanism study of brittle-to-ductile transition temperature in W-0.2 wt% Al_2O_3 alloy. J Mater Res Technol 2025;36:1672–82. https://doi.org/10.1016/j.jmrt.2025.03.246.
[188] Li L, Peng J, Tang S, Fang Q, Wei Y. Micromechanism of strength and damage trade-off in second-phase reinforced alloy by strain gradient plasticity theory. Int J Plast 2024;176:103970. https://doi.org/10.1016/j.ijplas.2024.103970.
[189] Yao L, Gao Y, Huang Y, Zhang G. Microstructure characterization and mechanical properties of Mo-Y_2O_3 alloys fabricated by hydrothermal synthesis and spark plasma sintering. Ceram Int 2025;51:40289–97. https://doi.org/10.1016/j.ceramint.2025.06.261.
[190] Ma M, Zhang S, Li K, Zhang W, Liu X, Li A, et al. Crack suppression in LPBF-processed W-ta-C alloys: synergistic roles of alloying and HIP-induced self-healing. Int J Refract Met Hard Mater 2026;134:107444. https://doi.org/10.1016/j.ijrmhm.2025.107444.
[191] Li T, Liu T, Zhao S, Chen Y, Luan J, Jiao Z, et al. Ultra-strong tungsten refractory high-entropy alloy via stepwise controllable coherent nanoprecipitations. Nat Commun 2023;14:3006. https://doi.org/10.1038/s41467-023-38531-4.
[192] Li Z, Pang J, Liu H, Zhu Z, Zhang L, Wang A, et al. Combined effect of silicon doping and thermal treatment on microstructures and mechanical properties of Ti50Nb20V20Al10 refractory high-entropy alloy. J Alloys Compd 2024;1005:176075. https://doi.org/10.1016/j.jallcom.2024.176075.
[193] Shu R, Mao Y, Martinez-Pechero A, Coenen JW, Terra A, Schönen S, et al. Study on the fracture behavior and toughening mechanisms of continuous fiber reinforced $W_f/Y_2O_3/W$ composites fabricated via powder metallurgy. Compos Part B Eng 2024;287:111845. https://doi.org/10.1016/j.compositesb.2024.111845.
[194] Gietl H, Olbrich S, Riesch J, Holzner G, Höschen T, Coenen JW, et al. Estimation of the fracture toughness of tungsten fibre-reinforced tungsten composites. Eng Fract Mech 2020;232:107011. https://doi.org/10.1016/j.engfracmech.2020.107011.
[195] Chen C, Chen Y, Li KL, Wang S, Zhang YF, Mao YR, et al. Interfacial microstructure and mechanical property of the discontinuous short tungsten fiber-reinforced tungsten matrix composites. Mater Charact 2024;215:114214. https://doi.org/10.1016/j.matchar.2024.114214.
[196] Chen Y, Chen C, Wang J, Wang S, Gong H, Mao YR, et al. The effect of Re on the microstructure and mechanical properties of tungsten fiber-reinforced tungsten composites. J Alloys Compd 2025;1042:184139. https://doi.org/10.1016/j.jallcom.2025.184139.
[197] Mao Y, Coenen J, Sistla S, Liu C, Terra A, Tan X, et al. Design of tungsten fiber-reinforced tungsten composites with porous matrix. Mater Sci Eng, A 2021;817:141361. https://doi.org/10.1016/j.msea.2021.141361.
[198] Hu Z, Liu Y, Wu J, Dong J, Ma Z, Liu Y. The simultaneous improvement of strength and ductility of the 93W-4.6Ni-2.4Fe prepared by additive manufacturing via optimizing sintering post-treatment. Addit Manuf 2021;46:102216. https://doi.org/10.1016/j.addma.2021.102216.
[199] Alam ME, Haag JV, Setyawan W, Henager CH, Odette GR. On the effect of high-temperature annealing on the microstructure and mechanical properties of a hot-rolled 90W7Ni3Fe tungsten heavy alloy. Mater Sci Eng, A 2024;896:146200. https://doi.org/10.1016/j.msea.2024.146200.
[200] Du F, Duan B, Wang D, Wu Z, Liu X. Preparation, microstructure and mechanical properties of a Ce-PSZ reinforced molybdenum alloy. Int J Refract Met Hard Mater 2025;131:107204. https://doi.org/10.1016/j.ijrmhm.2025.107204.
[201] Lin X, Huang L, Chang T, Xin T, Xue J, Liang J, et al. Enhanced mechanical property in molybdenum-rhenium alloy via high-temperature aging. J Alloys Compd 2025;1034:181251. https://doi.org/10.1016/j.jallcom.2025.181251.
[202] Yu L, Liang J, Li S, Zhang W, Xu H, Gao X, et al. Phase transformation from body-centred cubic to face-centred cubic in oxide dispersion strengthened (ODS) molybdenum-rhenium alloy. Scr Mater 2026;271:117018. https://doi.org/10.1016/j.scriptamat.2025.117018.
[203] Li C, Wang X-W, Su R-R, Hu X-X, Wei S-G, Tu H-J, et al. Deuterium distribution and behavior of blisters in pre-damaged and undamaged tungsten. Tungsten 2024;6:647–56. https://doi.org/10.1007/s42864-024-00262-4.
[204] Osetsky YN. Atomic-scale mechanisms of void strengthening in tungsten. Tungsten 2021;3:65–71. https://doi.org/10.1007/s42864-020-00070-6.

[205] Li Y, Cui D, Peng D, Ding Y, Wang Y, Sun Z, et al. Stable dislocation junctions empower superior radiation stability of dislocation arrays and subgrain boundaries. Scr Mater 2026;275:117163. https://doi.org/10.1016/j.scriptamat.2025.117163.
[206] Luo F, Luo H, Liu Q, Zhou L, Lin W, Xie Z, et al. The effect of rhenium content on microstructural changes and irradiated hardening in W-Re alloy under high-dose ion irradiation. Nanomaterials 2023;13:497. https://doi.org/10.3390/nano13030497.
[207] Wang X, Yang Q, Wu W, Zhang W, Zhang Y, Yan D, et al. Excellent radiation resistance via enforced local non-directional He diffusion in a WTaCrV multicomponent alloy containing coherent ordered nanoprecipitates. Acta Mater 2025;282:120501. https://doi.org/10.1016/j.actamat.2024.120501.
[208] Ji X, Luo G-N, Li Y, Fan C, Zhou H. Synergistic effects of rhenium alloying and ion channeling on helium irradiation blistering in tungsten: an in situ helium ion microscopy study. Nucl Fusion 2026;66:036047. https://doi.org/10.1088/1741-4326/ae463e.
[209] Huang J, Zhong Q, Chen Z, Cao Z, Ding Y, Zhou Z, et al. Effect of pre-existing dislocations and precipitates on microstructure evolution in W-0.5ZrC alloy during in-situ He^{+} & H^{2+} dual-beam synergistic irradiation. Int J Refract Met Hard Mater 2024;123:106777. https://doi.org/10.1016/j.ijrmhm.2024.106777.
[210] Wang J, Hatano Y, Toyama T, Hinoki T, Yabuuchi K, Zhang Y-F, et al. Irradiation effects on binary tungsten alloys at elevated temperatures: vacancy cluster formation, precipitation of alloying elements and irradiation hardening. Mater Des 2023;229:111899. https://doi.org/10.1016/j.matdes.2023.111899.
[211] Niu Y-Z, Li Y-H, Ma H-Z, Yang T-R, Hu X-X, Zhou H-B, et al. Influence of Re on the performance of W under irradiation: the critical role of introduction method and rate. J Mater Sci Technol 2026;241:123–37. https://doi.org/10.1016/j.jmst.2025.02.067.
[212] Li Y-H, Yue F-Y, Li Z-Z, Hou P-W, Niu Y-Z, Ma H-Z, et al. Temperature-dependent synergistic evolution mechanism of rhenium and irradiation defects in tungsten-rhenium alloys. J Mater Sci Technol 2023;145:221–34. https://doi.org/10.1016/j.jmst.2022.10.056.
[213] Yang T-R, Li Y-H, Ren Q-Y, Terentyev D, Xie H-X, Gao N, et al. Influence of rhenium-decorated dislocation loops on edge dislocation gliding in tungsten. Scr Mater 2023;235:115624. https://doi.org/10.1016/j.scriptamat.2023.115624.
[214] Gietl H, Koyanagi T, Hu X, Fukuda M, Hasegawa A, Katoh Y. Neutron irradiation-enhanced grain growth in tungsten and tungsten alloys. J Alloys Compd 2022;901:163419. https://doi.org/10.1016/j.jallcom.2021.163419.
[215] Ma X, Zhang X, Wang T, Gao Y, Yuan Y, Cheng L, et al. Decreased surface blistering and deuterium retention in potassium-doped tungsten exposed to deuterium plasma following ion irradiation. Nucl Fusion 2023;63:026013. https://doi.org/10.1088/1741-4326/aca48c.
[216] Wang X, Huang H, Shi J, Xu H-Y, Meng D-Q. Recent progress of tungsten-based high-entropy alloys in nuclear fusion. Tungsten 2021;3:143–60. https://doi.org/10.1007/s42864-021-00092-8.
[217] Hatler C, Robin I, Kim H, Curtis N, Sun B, Aydogan E, et al. The path towards plasma facing components: a review of state-of-the-art in W-based refractory high-entropy alloys. Curr Opin Solid State Mater Sci 2025;34:101201. https://doi.org/10.1016/j.cossms.2024.101201.
[218] Pu G, Wang Y, Wang S, Chen S, Gan L, Zhong R, et al. Size-dependent irradiation tolerance and mechanical properties in WTaTiVCr/W multilayered films. Int J Refract Met Hard Mater 2024;121:106637. https://doi.org/10.1016/j.ijrmhm.2024.106637.
[219] Supakul S, Robin I, Aydogan E, Chen W-Y, Vigil M, Sun B, et al. Bulk synthesis of radiation resistant W – ti – cr – v compositionally complex alloys. J Mater Res Technol 2025;39:4780–93. https://doi.org/10.1016/j.jmrt.2025.09.046.
[220] Wu X, You Y-W, Kong X-S, Chen J-L, Luo G-N, Lu G-H, et al. First-principles determination of grain boundary strengthening in tungsten: dependence on grain boundary structure and metallic radius of solute. Acta Mater 2016;120:315–26. https://doi.org/10.1016/j.actamat.2016.08.048.
[221] Kong X-S, Song C, Chen L, Xie Z-M, Liu C-S, Hou J. First-principles study of substitutional solute and carbon interactions in tungsten. Tungsten 2022;4:231–8. https://doi.org/10.1007/s42864-022-00145-6.
[222] Li Y, Ran G, Guo Y, Sun Z, Liu X, Li Y, et al. The evolution of dislocation loop and its interaction with pre-existing dislocation in He+-irradiated molybdenum: In-situ TEM observation and molecular dynamics simulation. Acta Mater 2020;201:462–76. https://doi.org/10.1016/j.actamat.2020.10.022.
[223] Wang T, Wang X, Ma X, Cheng L, Yuan Y, Guo W, et al. Neon-concentration dependent retarding effect on the recrystallization of irradiated tungsten: experimental analysis and molecular dynamics simulation. J Mater Sci Technol 2023;139:245–59. https://doi.org/10.1016/j.jmst.2022.09.031.
[224] Hu Y, Li Z, Xu X, Zhang Y, Xia R. Shock wave dynamics in nanoporous tungsten and molybdenum via molecular dynamics simulations: insights into thermodynamic and structural evolution. J Mater Res Technol 2025;35:558–69. https://doi.org/10.1016/j.jmrt.2025.01.074.
[225] Afaneh F, Khattari ZY, Al-Buriahi MS. Monte carlo simulations and phy- X/PSD study of radiation shielding and elastic effects of molybdenum and tungsten in phosphate glasses. J Mater Res Technol 2022;19:3788–802. https://doi.org/10.1016/j.jmrt.2022.06.125.
[226] Zhong Z, An J, Wu D, Gao N, Liu L, Wang Z, et al. A machine learning strategy for enhancing the strength and toughness in metal matrix composites. Int J Mech Sci 2024;281:109550. https://doi.org/10.1016/j.ijmecsci.2024.109550.
[227] Cheng Y, Shu R, Sun H, Zou M, Jiao Y, Wu Z, et al. Machine learning-assisted interfacial modulation and configuration design of metal matrix composites: a review. Mater Today Commun 2025;46:112504. https://doi.org/10.1016/j.mtcomm.2025.112504.

Yijia Wang (First Author) is currently pursuing a master's degree in Materials and Chemical Engineering at the School of Materials Science and Engineering, Southwest Jiaotong University, China. Her research focuses on the fabrication and microstructural control of tungsten-based alloys and composites, their interfacial behavior, and the strengthening and toughening mechanisms of refractory metallic materials.

Rui Shu (Corresponding Author) is currently an associate research fellow at the School of Materials Science and Engineering, Southwest Jiaotong University, China, where he supervises master's students. He received his Ph.D. in Mechanical Engineering from RWTH Aachen University in 2024. His current research focuses on powder metallurgy and metal matrix composites, particularly the fabrication, microstructural evolution, interfacial behavior, and mechanical performance of refractory-metal composites. As first author, he has published papers in leading international journals, including Carbon, Composites Part A: Applied Science and Manufacturing, Composites Part B: Engineering, and Materials Science and Engineering: A. To date, he has published more than 70 SCI-indexed papers, including 26 as first or corresponding author. Collectively, his publications have received more than 900 citations.

Xiaosong Jiang (Corresponding Author) is a professor and vice dean of the School of Materials Science and Engineering at Southwest Jiaotong University, China. He received his bachelor's degree in powder metallurgy from Central South University, his master's degree in materials physics and chemistry from Southwest Jiaotong University, and his Ph.D. in materials science from Tongji University. His research focuses on powder metallurgy and metal matrix composites. At present, he has been listed as the first author or corresponding author to publish more than 150 SCI indexed papers, such as Carbon, Composites Part A:Applied Science and Manufacturing, Composites Part B: Engineering, Materials Science & Engineering A, etc. More than 70 papers have an impact factor greater than 5.0 and all of them have been cited over 3600 times (H-index of 33). As the first patent holder, 17 Chinese invention patents have been authorized. He published “Fundamentals and Applications of Failure Analysis of Metal Material Components” as the first editor in chief. Served as an editorial board member for the journal “Reviews on Advanced Materials Science” (JCR Q2, IF = 5.1), as well as for “Mechanical Engineering Materials” and “Powder Metallurgy Materials Science and Engineering".